Direct 3D Numerical Simulation of Shear Gravitational Turbulent Mixing

Sin'kova O.G., Statsenko V.P., Yanilkin Yu.V.

Paper to be presented at International Workshop on Physics of Compressible Turbulent Mixing (Cambridge, July 2004)

3D code TREK is used to study turbulence growth in the gravitational field at a plane interface of two incompressible fluids of density difference n=3 with initial velocity shift at the interface. The case is addressed where the acceleration sign corresponds to stable stratification. The computed data is compared to computations by a phenomenological model.

This paper addresses the problem of turbulent mixing at a plane interface of two incompressible fluids under action of velocity shear and acceleration creating a stable situation. This kind of flow occurs, for example, in the upper or lower part of the initial portion of plane or round jets of a density other than the surrounding jet density.

Previously we studied simplest flows with gravitational [1] or shear [2] instabilities. The flow under study here represents a more complex case and is both of independent interest since such flows are abundant in the nature and of interest as a test for semiempirical turbulence models.

The above problem was studied previously in refs. [3,4] using Nikiforov's turbulence model and the $k-\varepsilon$ model. The results reduced only to the time dependency of the turbulent mixing zone (TMZ).

This paper studies the problem of interest with the DNS method of direct numerical simulations using 3D gas-dynamic code TREK [5]. Both the computational grid and the numerical method are varied: in one approach the materials were considered as different, that is, of different concentrations; in the other as a single material, without singling-out with volume concentrations.

Besides, we also study this problem numerically using the phenomenological $k-\varepsilon$ turbulence model [6]. The time dependence not only of the TMZ width, but also of maximum turbulent energy in the TMZ has been considered.

Numerical arrays of hydrodynamic quantities from 3D computations are used for determination of moments of the quantities (Reynolds tensor diagonal components, turbulent flows, profiles of density and its mean-square fluctuation) as well as construction of the one-point concentration probability distribution density function (PDF) and spectral analysis of the velocity and density fluctuations.

Some results of the 3D computations are compared to measurements [7-9] and the data of semiempirical theory of turbulence [10] that accounts for the Reynolds tensor anisotropy.

1. Setting up the TREK computations

The problem is formulated (similar to [1,2]) as follows. At the initial time two half-spaces separated by plane z= z_c =0 are filled with ideal gases at rest of densities ρ_1=1 and ρ_2=n (n=3, Atwood number $A \equiv \frac{\rho_2 - \rho_1}{\rho_2 + \rho_1}$). The initial geometry is presented in Fig. 1. The velocity is $u_{y1} \equiv u_y(z > 0) = -0.5$ in the upper half-plane and $u_{y2} \equiv u_y(z < 0) = 0.5-$ in the lower.Gravity g_z is directed from the light material to the heavy. Its value was varied from $g_z = 0.2$ to $g_z = 1$. At the initial time, random density perturbations $\delta\rho = \pm \rho_1 \cdot \delta$, where δ= 0.1, are given using the random-number generator at the interface (in a layer one cell thick). Gas-dynamics equations for ideal two-material medium (with zero molecular viscosity and heat conduction) are solved. The computational domain is a parallelepiped, with its vertical side of the side face being L_z=1. Its horizontal face is a square with side $L_x = L_y$ =1.

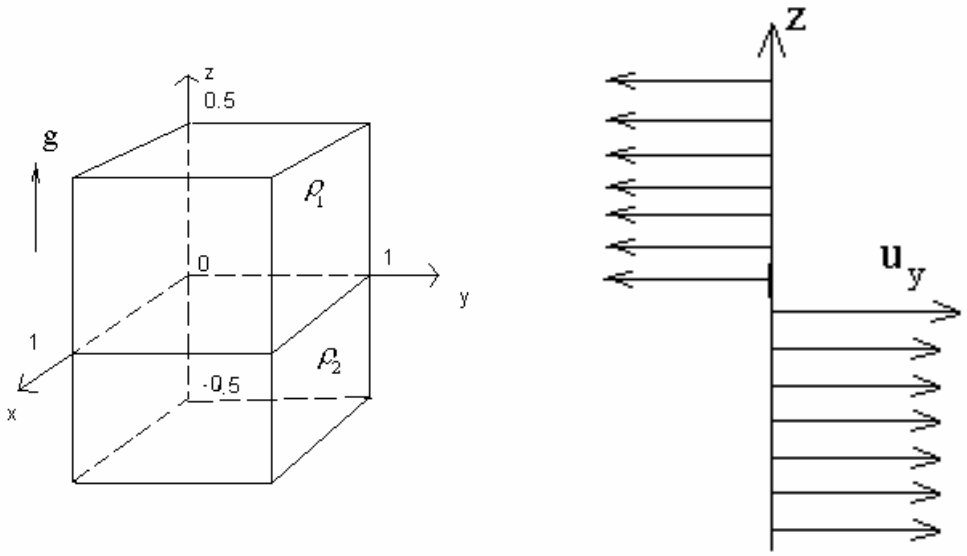

Fig. 1. Geometry of the problem

The initial pressure profile was given reasoning from the hydrostatic equilibrium condition:

$$p(z) = p_0 - \int_{z_2}^{z} \rho(z) \cdot g \cdot dz \,.$$

Here the coordinate of the upper face is z_2 = 0.5, that of the lower face z_1 = -0.5, p_0 =15.4. Note that the pressure (p ≈ p_0) is such, that the following non-compressibility condition was met well for the turbulent flow k=ξLtg<<γp/ρ, where ξ=const<<1, L_t <Λ, L_t is the turbulent mixing zone (TMZ) width, k is the turbulent energy.

The equation of state is ideal gas with adiabatic constant γ=1.4.

The computational grid is uniform with $N_x = N_y = N_z$ cells. The number of the cells was varied from N_x=100 to N_x=200. The cell size is $h_x = h_y = h_z = 1/N_x$. With the above computational grid options the problem was calculated with two concentrations, that is the two gases of different density were considered as different materials.

On the computational grid with N_x=100 the problem was also calculated with a single concentration, that is, the two gases of different density were considered as one and the same material.

The "rigid wall" condition was posed on the horizontal boundaries of the computational domain and the periodicity condition on the vertical.

2. Results of 3D computations

2.1 2D sections

The general idea of the flow evolution in this problem is provided by the raster patterns of the heavy material concentration from the 3D computation on coarser (N_x=100) and finer (N_x=200) grids, see Figs. 2 through 8 depicting the longitudinal 2D sections (along the flow) of the computational domain.

At the first stage of the problem, shear instability is dominating and the vortex enlargement with time is observed. A feature of the flow is the curling of the vortices drawing their circulation from the averaged flow with velocity shear. On a fine enough grid there should be tapering-off to the relevant self-similar regime at the end of the stage.

At the second stage, a stable stratification of the problem begins to show up that inhibits the perturbation growth due to shear instability and the vortex stabilization is observed. Time scale t_0 characteristic of this stage as well as space scale L_0 can be introduced that are determined by velocity shear $\Delta u_y \equiv \left| u_{y1} - u_{y2} \right|$ and gravity g_z:

$$t_0 = \Delta u_y / g_z ,$$

$$L_0 = (\Delta u_y)^2 / g_z .$$

Thus, till width L_t of the TMZ is small in comparison with L_0, the gravity can be neglected. If the computational domain size L_z is also small in comparison with L_0, we obtain the problem of pure shear mixing. Otherwise ($L_z >> L_0$), too few cells fall on the TMZ. In our computations $\Delta u_y = 1$, hence, the L_0 optimal for that problem was selected by variation of the g_z.

In the above computations $g_z = 0.2$, therefore the plots presented cover both the stages.

The raster patterns of the velocity components in the 3D computation with single material on grid N_x=100 are shown in Fig. 9 for time τ=2, when the gravity effect is significant.

2.2 Mixing zone

At the first (unstable) stage of the problem, there should be the tapering-off to the self-similar regime. It is characterized with a linear time dependence of the TMZ width:

$$L_t = L^{(0)} + \alpha \cdot \Delta u_y \cdot t\,.$$

Here $L_t \equiv z_2 - z_1$, is the TMZ width in z direction that is determined from points z_1, z_2, at which small enough value ε of an averaged hydrodynamic quantity, for example, heavy material concentration **c** or velocity u_y, is reached. In the first case we assume in what follows that

$$c_2(z_1)=\varepsilon,\ c_2(z_2)=1-\varepsilon,$$

where c_2 is the mass fraction of the material of initial density ρ_2=n; denote the resultant L_t by $L_t^{(c)}$. In the second case we assume in what follows that

$$\left|2u_y(z_2) - \Delta u_y\right| = \varepsilon,\ \left|2u_y(z_1) + \Delta u_y\right| = \varepsilon\ ;$$

denote the TMZ width by $L_t^{(u)}$.

Evidently, in view of the previous section, the scaled TMZ width is:

$$l_t \equiv \frac{L_t}{L_0} = l^{(0)} + \alpha \cdot \tau\,, \quad \text{where: } \tau \equiv t / t_0\,. \quad (1)$$

Thus, self-similar dependence (1) with small enough $l^{(0)}$ must be of a universal form at the next stage as well and independent of $\Delta u_y, g_z$. Precisely this can be seen in Fig. 10 plotting $l_t(\tau)$.

Note that in the 3D computation variant for N_x=100 with two materials when $\tau > 2.5$ the influence of the computational domain boundaries begins to show up (see also below).

That same figure plots the straight lines, whose slopes correspond to the maximum and minimum rates of the TMZ width growth at the self-similar stage of the shear flow among their most probable values measured in refs. [7,8] as well as in different experiments presented in ref. [9].

It is seen that at the initial stage of the 3D computations with two materials ($\tau \lesssim 1$) there is the tapering-off of the $l_t(\tau)$ to linear dependencies characterized with slopes close to the experimental ones, with $l_t^{(u)} \approx l_t^{(c)}$. At a later stage ($\tau \gtrsim 1$) the slope of the curves $l_t(\tau)$ begins to decrease and the $l_t^{(u)}$ becomes noticeably larger than $l_t^{(c)}$. The variants on different grids are

close to each other on the whole, the difference is mainly in a minor delay (shift in time) in the computation on a coarser grid.

In the 3D computation with a single material the delay (shift in time) is even more noticeable, moreover, at a late stage the $l_t^{(u)}$ and $l_t^{(c)}$ are close on the whole as before.

Note that when t>2.5-3 the influence of the computational domain boundary on the side of the light material begins to show up.

2.3 Time change of fluctuation characteristics

For the first stage of this problem the self-similar regime also manifests itself in the tapering-off to the steady value of

$$k_m(t) \equiv \max(k),$$

maximum turbulent energy over the TMZ width, where:

$$k(z) = k_{ii},$$

$$k_{ik}(z) = \frac{< u_i u_k > - < u_i >< u_k >}{2};$$

the averaging (denoted by <>) is performed over the whole horizontal section z=const.

As seen from Fig. 11, k_m(t) from the computation on a fine grid by $\tau \approx 0.5$ is close to the values measured in experiments [7,8]. When $\tau > 1$, it decreases. In a computation on a coarser grid, the behavior of $k_m(t)$ is much alike on the whole, the difference is mainly a slight delay (time shift).The same is observed in the 3D computation with single material, here the delay (time shift) is even larger.

Fig. 12 plots the time curve of the velocity fluctuation anisotropy taken in the middle of TMZ

$$E_{ij}(t) \equiv k_{ii} / k_{jj}, \qquad (2)$$

where diagonal components k_{ii} (here there is no summation over **i**) of tensor k_{ik} (in (2) there is no summation over subscripts i, j) appear that are maximum over the TMZ width. As seen from Fig. 12, Reynolds tensor anisotropy takes place in the 3D computations, with the “longitudinal” component k_{yy} of the diagonal part of tensor k_{ij} in the mixing zone being larger than the “transversal” ones in the two-material computations.

According to the turbulence model [10] that includes the Reynolds tensor anisotropy, the following relations are valid for the initial stage:

$$E_{zy} \equiv \frac{k_{zz}}{k_{yy}} = \frac{1/3 - b}{1/3 + 2b}, \qquad (3)$$

$$E_{xz} \equiv \frac{k_{xx}}{k_{zz}} = 1 \quad .$$

The E_{zy} is given in Fig. 12 for two values of b=0.13 and b=0.085 – these values describe the previously studied flow best. As seen from Fig.12, the results for E_{ik} agree on the whole with (3) to an accuracy of fluctuations both in the two-material variants and in the single-material calculation (at some delay in this case).

Fig. 13 plots the time curve of TMZ-maximum squared density fluctuations R_m

$$R_m \equiv \max(< \rho'^2 >) .$$

As follows from the Fig. 13, at the first stage of the 3D computation, the values of R_m in the single concentration computations are significantly lower than those in the computations with two concentrations. At the next stage, in the single-fluid computation, the values of R_m drop. In the two-fluid 3D computation, these values remain essentially constant – the situation is similar to the case of the acceleration discussed in ref. [11].

Fig. 14 plots the time curve of TMZ-maximum (modulo) turbulent mass flow:

$$R_{zm} \equiv \begin{cases} \max\left(R_z\right), & R_z > 0 \\ -\max\left(-R_z\right) & R_z < 0 \end{cases} \qquad \text{where: } R_z \equiv < \rho' u_z' > \ .$$

Like for k_m, from Fig. 14 it follows that at the end of the first stage, the R_{zm}'s taper off to a value close in all the variants. At the next stage the positive turbulent flow abruptly decreases and a negative flow appears, with severe fluctuations being observed. On the whole, the behaviors of $R_{zm}(t)$ are close in all the variants, except for the time shift already mentioned.

2.4 Profiles of the quantities

Fig. 15 compares the turbulent mass flow profiles $R_z \equiv < \rho' u_z' >$ from the 3D computations. At the end of the first stage the profiles are quite close. Then their amplitude deceases (as mentioned above, with some time delay in the single-material computation). In so doing the most noticeable decrease is in the heavy material TMZ, it is precisely there, where negative values of R_z appear by time τ~1.6.

16a ÷ 18a plot the profiles of velocity, density, and turbulent energy from both one-material and two-material computations, Figs. 16b ÷ 18b the profiles of Richardson number

$$Ri \equiv g_z \frac{\partial \rho}{\partial z} \Big/ \rho \left(\frac{\partial u_y}{\partial z} \right)^2 .$$

As seen from the figures, at the first stage the velocity and density profiles are close in their shape and position, with taking into consideration the time shift in the single-material computation. However, for $\tau>1.4$ in this computation, unlike in the two-material computation, a shelf forms in the density profile. Accordingly, the peak turbulent energy near the shelf proves higher, as it would be expected with taking into account that the velocity profiles are therewith close in the two variants.

As seen from Figs. 16b ÷ 18b, at the end of the first stage the Richardson number profiles bear a qualitative resemblance, that is: in the heavy material region they produce a "barrier" inhibiting turbulence and impeding the material and vorticity penetration into the region (recall that the critical value of the Reynolds number is $Ri \sim 0.5$). This accounts for the dominant expansion of the velocity and density profiles toward the light material: the resultant asymmetry becomes noticeable, as compared to the unstable stratification.

2.5 Concentration probability distribution density function

The data from the numerical computation has been used to determine the one-point heavy material mass concentration probability distribution density function

$$F(c_2, z, t) = \frac{N(c_2^{(ik)}(z) \geq (c_2 + \Delta c)) - N(c_2^{(ik)}(z) \geq c_2)}{N_0 \Delta c},$$

here $N(c_2^{(ik)}(z) \geq c_2)$ is the number of points in a given horizontal plane z, at which the current concentration $c_2^{(ik)}$ is larger than c_2, $N_o(z)$ is the total number of points in the plane. The c_2 runs a range of M numbers

$$c_2 = (0, \quad 1, \quad 2, \quad ...., \quad M-1)\Delta c,$$

where $M\Delta c = 1$; in our computations, M=100.

Fig. 19 plots the functions $F(c_2)$ calculated from the source array (without averaging) of the concentrations c_2 for the TMZ region close to the light material at times $\tau=1$ (the end of the first stage) and $\tau=2$ (a noticeable inhibition of the turbulence) in the two-material computation performed on a fine grid (N_x=200). The figure plots the vertical coordinate z (counted from the interface) divided by TMZ width L_t, that is: $\eta \equiv \frac{z - z_c}{L_t}$. As the curves for $\tau=1$ and $\tau=2$ are taken for the same z, the relevant η_1 and η_2 prove different. The maximum values of the function $F(\mathbf{c_2})$ can be seen to be achieved mainly near $\mathbf{c}\approx1$ and $\mathbf{c}\approx0$, that is, the $F(c_2)$ is concentrated (is of the form of the δ-function) at the extreme points of the concentration range. However, in the major range of $\mathbf{c_2}$ its value is low ($F(\mathbf{c_2})<0.1$-0.2); physically, this is close to immiscible fluids, which is characteristic of problem descriptions using 3D computations with two concentrations (see also [11]).

Next, before we find F(**c₂**), average the concentration array with the formula:

$$c_2^{(n)}(l,x,y,z) = \langle c_2 \rangle_{|_{l,x,y,z}}; \qquad n = 1,2....N_z$$

where l=rh, r=2 , when r≥2 (but r<<min(N_x,N_y)), the resultant functions F(**c₂**) differ slightly, whereas for r=1 the difference is radical: as we have seen, the F(**c₂**) is close to two δ-functions, δ(0) and δ(1).

Now find F(**c₂**) with averaging of the initial concentration array assuming r=2 .

Figs. 20 and 21 compare thus found functions F(c_2) for times τ=1 and τ=2, for two computation variants: with one and two materials, with the latter being on a fine grid (N_x =200).

From Figs. 20 it is seen that in the TMZ region adjacent to the heavy material ($\eta \tilde{<} -0.2$), the maximum values of F(c_2) are achieved closer to c_2≈1, that is, the heavy material particles are most probable. A close behavior of the F(c_2) is in the two-material computation.

A noticeable discrepancy between the above variants begins in the central TMZ part adjacent to the light material: in the single-material computation the maximum F(c_2) is achieved in the middle of the c_2 values, whereas in the two-concentration variant the F(c_2) proves concentrated to a large extent near the end values of the c_2 range, although not so significantly as for r=1 – the characteristic value within the interval: c_2≈0.5.

Finally, in the TMZ region adjacent to the light material ($\eta > 0.2 \div 0.3$) the maximums of F(c_2) are achieved closer to c_2≈0 in either computation, that is, the light material particles are most probable.

2.6 Velocity and density fluctuation spectra

As known [12], the average squared fluctuation of the i-th velocity component $\overline{u_i'^2}$ (with no summation over i) is related to the associated one-dimensional spectral density $\tilde{E}_i(k)$ as:

$\overline{u_i'^2} = \int_0^\infty \tilde{E}_i(k')dk'$. Note that in our case the averaging over ensemble corresponds to that in the horizontal plane X,Y. Hence, $\overline{u_i'^2}$ is a function of **z**.

Following [12], relate any fixed k to division of energy $\overline{u_i'^2}$ into two parts:

$$\overline{u_i'^2} = \int_0^k \tilde{E}_i(k')dk' + \int_k^\infty \tilde{E}_i(k')dk'.$$

This division is correspondent with the division of the field of prompt values u_i into macrocomponent $\overline{u}_i$ (with energy $\int_0^k \tilde{E}_i(k')dk'$) and microcomponent $\underline{u}_i$ (with energy

$E_i(k) = \int_k^\infty \tilde{E}_i(k')dk'$), see ref. [12]. In ref. [12], $\tilde{E}_i(k')$ is referred to simply as a spectrum – one-dimensional spectral density of field u_i that corresponds to the correlation function of this field is meant. Kolmogorov spectrum takes place in the inertial turbulence interval: $\tilde{E}_i(k') \sim (k')^{-5/3}$.

It is our view that $E_i(k)$ has a more profound physical meaning. It determines doubled specific kinetic energy of fluctuations of the i-th velocity component of wavelength $\lambda \le \frac{2\pi}{k}$. The Kolmogorov spectrum for $\tilde{E}_i(k')$ as well as for the total energy of all components $E(k) \equiv \sum_i E_i(k) \sim k^{-2/3}$ is evidently correspondent with dependency $E(k) \sim E_i(k) \sim k^{-2/3}$, we will also term it the Kolmogorov spectrum of turbulent energy $E(k)$ and its components $E_i(k)$.

The computed data was used as a basis to study the spectrum of the turbulent energy and its components in accordance with formula

$$\begin{aligned} &E_i^{(n)}(l,x,y,z) = \langle u_i^2 \rangle_{|_{l,x,y,z}} - \langle u_i \rangle^2_{|_{l,x,y,z}}; \qquad n = 1,2....N_z \\ &E_i(l,z) = \langle E_i^{(n)}(l,x,y,z) \rangle; \qquad l = rh, \qquad r = 2,3....N_x. \end{aligned} \quad . \tag{4}$$

Here the averaging $\langle\rangle_{|_{l,x,y,z}}$ is performed in the n-th layer (over z) in a square with side l (l=rh, h is the computational cell size), whose center coordinates are x, y, z, and then the averaging ($\langle\rangle$) is over all possible values of x, y in the squares with the value of l, z in the entire n-th layer. There is no summation over **i** in (4). Next

$$E(l,z) = \sum_{i=1}^{i=3} E_i(l,z) \quad .$$

The computed data for several times in the computation on the grid with N_x=201 are presented in Figs. 22, 23 as curves $\lg E_i(\lg k)$, $\lg E(\lg k)$ (where k=2π/l) for different values of the scaled coordinate $\zeta \equiv \frac{z - z_c}{L_t}$.

The figures also present the Kolmogorov spectrum of turbulent energy

$$\lg E = -\frac{2}{3}\lg k + const\,.$$

As seen, inside the TMZ (0.4> ζ > -0.4) there are intervals of wave numbers K, on which the spectrum of total energy E is close on the whole to the 3D Kolmogorov spectrum. However, for some components the difference from the Kolmogorov dependency is significantly larger. Note that for large space scales (low K) E_y is dominant, as it must for the shear flow according to the phenomenological model [10] and the measurements [7,8]. However, for small

scales (high K) E_x is dominant at nearly all TMZ points. A most apparent reason is the action of the scheme viscosity, which is noticeable just for small scales and inhibits precisely the components E_y, E_z, as for large scales it is y and z that are the major velocity directions generating the anisotropic scheme viscosity in small scales. Note that, as seen from Figs. 22 and 23, the anisotropy increases from the center of the TMZ to its edges, as the velocity module determining the scheme viscosity also increases. A similar scheme viscosity effect is treated in more detail in ref. [13].

A similar spectral quantity is calculated for the squared density fluctuations:

$$R_l^n(x,y) = \langle \rho^2 \rangle_{|_{l,x,y,z}} - \langle \rho \rangle^2_{|_{l,x,y,z}} \qquad ; \qquad n = 1, 2 \ldots . N_z$$

$$R_l(z) \equiv \langle R_l^n(x,y) \rangle \qquad ; l = rh, \quad r = 2, 3 \ldots . N_x ;$$

it is shown in Figs. 24 through 26. The figures also present the Kolmogorov spectrum of the squared density fluctuations (see also ref. [12])

$$\lg R_l = -\frac{2}{3} \lg k + const .$$

As seen from Fig. 24, at the first stage (τ=0.6), when the mixing is mainly of the shear nature, in small scales the spectrum is close to the Kolmogorov spectrum in the 3D computations. The best agreement is observed for negative scaled coordinate ζ, that is, in the region of the heavy material; in the region of the light material a deviation from the Kolmogorov spectrum becomes noticeable.

At the next stage (τ=1.2), when the shear mixing begins to be inhibited due to stable stratification, as it is seen from Fig. 25, the density spectrum begins to differ more significantly from the Kolmogorov spectrum, with this being to a greater extent in the light material region. The difference of the spectrum from the Kolmogorov spectrum is even larger for a later stage (τ=1.8) depicted in Fig. 26.

This agrees with the concepts of ref. [12] about the density spectrum behavior for immiscible fluids given the stable stratification leading to the change of sign in the turbulent mass flow.

3 Results of $k - \varepsilon$ computations

Fig. 10 plots the time curve of the TMZ width from the $k - \varepsilon$ calculations for several values of $g_z = 0.2$, 0.4, 1. As it would follow from the conclusions of Section 2.2, all the curves of scaled $l_t(\tau)$ are close for these values, that is, are of a universal form independent of g_z.

At the initial stage (τ<1-1.5) the slope of the curves is close both to the 3D computations and to the associated experimental data as well to the data of refs. [3,4].

At the following times the slope decreases, like in the 3D computations, but, in contrast to them, in the $k-\varepsilon$ computations there is no boundary effect. In the variant most advanced in τ with g=1, there is essentially no growth in $l_t^{(c)}$, while $l_t^{(u)}$ tapers off to the linear dependence on τ ; in so doing, however, the angle of slope of $l_t^{(u)}(\tau)$ is much smaller (by about an order of magnitude) than that at the first stage. The maximum values are $l_t^{(c)} \approx 0.36, l_t^{(u)} \approx 0.5$, which agrees with the data of refs. [3,4], i.e. $l_t \approx 0.45$.

The time histories of turbulent energy k_m (t) maximum in the TMZ width in the $k-\varepsilon$ computations and in the 3D computations are quite close (Fig. 11), providing the delay (shift in time) in the latter is taken into account. In the variant most advanced in τ with g=1, k_m (t) tapers off to an essentially constant value, which is lower by about an order of magnitude than that at the first stage.

Figs. 16a÷18a plot velocity, density and turbulent energy profiles from the $k-\varepsilon$ computations and Figs. 16b ÷ 18b Richardson number profiles. As seen from the figures, at the first stage the velocity and density profiles are close in their shape and position to those from the 3D computations with taking into consideration the time shift. For τ>1.5 the turbulent energy profiles from the $k-\varepsilon$ computation are closer to those in the 3D computation on the fine grid, although are somewhat wider, which is due in part to the time shift in the latter.

The Richardson number profiles, as seen from Figs. 16b ÷ 18b, are also much like those from the 3D computation on the fine grid, in particular, in the region of the heavy material, where they form a turbulence inhibiting "barrier" (see Section 2.4).

Conclusions

The results of the TREK direct 3D numerical simulation of the turbulent shear gravitational mixing with stable stratification were as follows.

At the first (unstable) mixing stage, when the shear turbulence generation is prevailing, the TMZ width behavior is much alike in all the computations and agrees with the associated experimental data [7-9] as well as the data of computations [3,4] by the phenomenological model.

The TMZ-maximum scaled turbulent energy E_m (agreeing with the experimental data [7-8]) and turbulent mass flow achieved at the end of the first stage are also close in all the computations, while the TMZ-maximum squared density fluctuations are significantly lower in the computations with one concentration than in those with two concentrations.

The second (stable) stage, where the turbulence is inhibited, proceeds with $\tau \tilde{>} 1-1.5$. It is correspondent with decrease in the TMZ width growth rate and noticeable decrease in

turbulent energy E_m. The TMZ-maximum values R_m of the squared density fluctuations also decrease in the single-fluid computation. In the 3D two-fluid computation these values remain essentially constant: the situation is similar to the case of the alternating-sign acceleration discussed in ref. [11].

Inside the TMZ, in the single-material computation the one-point heavy material mass concentration probability distribution density function $F(c_2)$ achieves its maximum in the middle of the c_2 range, whereas in the two-material computation the $F(c_2)$ proves largely concentrated near the extremes of the c_2 range.

In the $k-\varepsilon$ computations, the TMZ width growth rate at the initial stage is close to the 3D computations and measurements. The decrease in the rate at the next stage agrees qualitatively with the 3D computations. The nature of the decrease in the turbulent energy E_m at that stage is also close to the 3D computations.

The authors are thankful to V.A. Zhmailo for his valuable comments.

References

1. Yanilkin Yu.V., Statsenko V.P., Rebrov S.V., Sin'kova O.G., Stadnik A.L. Study of gravitational turbulent mixing at large density differences using direct 3D numerical simulation // Report to 8th International Seminar on Turbulent Mixing of Compressible Matter. 8th IWPCTM, Pasadena, USA, 2001.
2. Stadnik A.A., Statsenko V.P., Yanilkin Yu.V., Zhmailo V.A. Direct numerical simulation of turbulent mixing in shear flows // Laser and Particle Beams, Vol.15, N 1, 1997-2. pp.115-125.
3. V.A. Andronov, I.G. Zhidov, E.E. Meshkov et al., Computational and Experimental Studies of Hydrodynamic Instabilities and Turbulent Mixing (Review of VNIIEF Efforts), Los Alamos National Laboratory report LA-12896, UC-700 1995.
4. Nikiforov V.V., Yanilkin Yu.V., Yudin Yu.A. et al. Numerical Simulation of Turbulent Mixing in Two-Dimensional Flows. The Phisics of Compressible Turbulent Mixing, Marseille (France), 374-380, 1997.
5. Yanilkin Yu.V., Tarasov V.I., Stadnik A.L. et al. Program System TREK for Numerical Simulation of 3D Multi-component Medium Flows. Proceedings of workshop «New Models and Numerical Codes for Shock Wave Processes in Condensed Media», Oxford, 1997, pp 413-422, 1997.
6. G.M. Eliseyev, V.Yu. Shemyakin, V.P. Statsenko, V.I. Tarasov, Yu.V. Yanilkin, G.V. Zharova. Turbulent combustion of hydrogen-air mixture in a closed vessel. //

Report to 7th International Seminar on Turbulent Mixing of Compressible Matter. 7th IWPCTM, St, Petersburg, Russia, 1999, pp.244-251.

7. Spenser B.W., Jones B.G. Statistical investigation of pressure and velocity fields in the turbulent two-stream mixing layers . -AIAA Paper, 1971, P.613.
8. Browand F.K., Latigo B.O. Growth of the two-dimensional mixing layer // Phys.Fluids. 1979. Vol. 22, N 6, pp.1011.
9. Rodi W.A. Rewiew of experimental data of uniform density free turbulent boundary layers. -Studies in convection, Acad. Press, London, 1975, Vol 1, pp.79-166.
10. Statsenko V.P. Testing of the turbulence model with Reynolds tensor anisotropy// Voprosy Atomnoy Nauki i Tekhniki, Ser. Teoreticheskaya i Prikladnaya Fizika, 1996, pp.43-51.
11. Sin'kova O.G., Sofronov V.N., Statsenko V.P., Yanilkin Yu.V., Zhmailo V.A.. Numerical study of the gravitational turbulent mixing in alternative-sign acceleration// Paper to be presented at International Workshop on Physics of Compressible Turbulent Mixing (Cambridge, July 2004).
12. A.S. Monin, A.M. Yaglom. Statistical hydromechanics, Part 2, Moscow, Nauka Publishers, 1967.
13. Sin'kova O.G., Statsenko V.P., Yanilkin Yu.V., Guzhova A.R., Pavlunin A.S.. Numerical simulation of an experiment to study turbulent mixing on multiple shock wave passage through interface// Paper to be presented at International Workshop on Physics of Compressible Turbulent Mixing (Cambridge, July 2004).

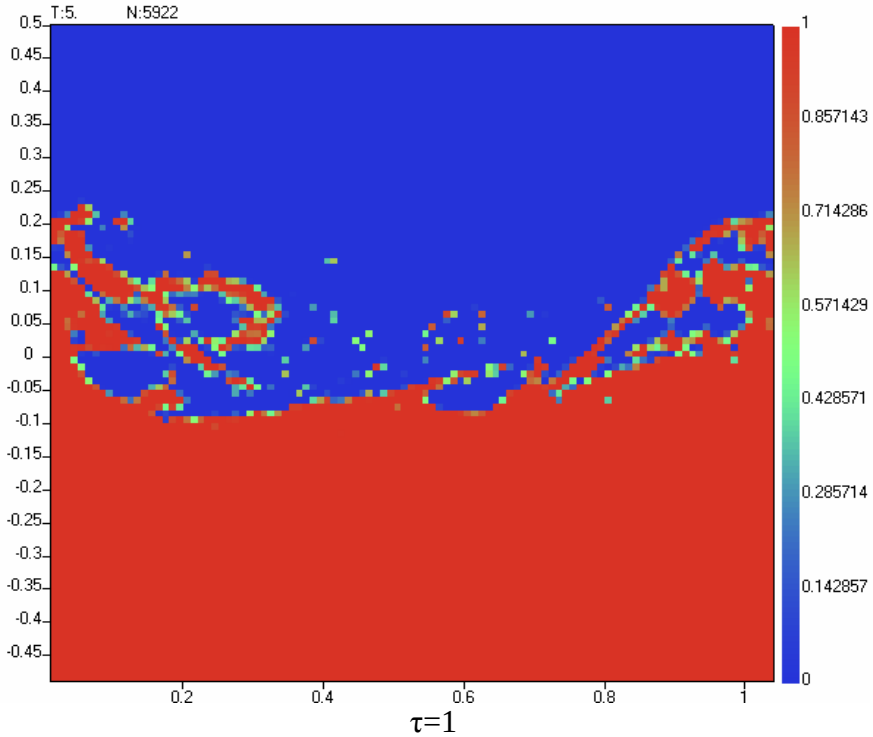

τ=1

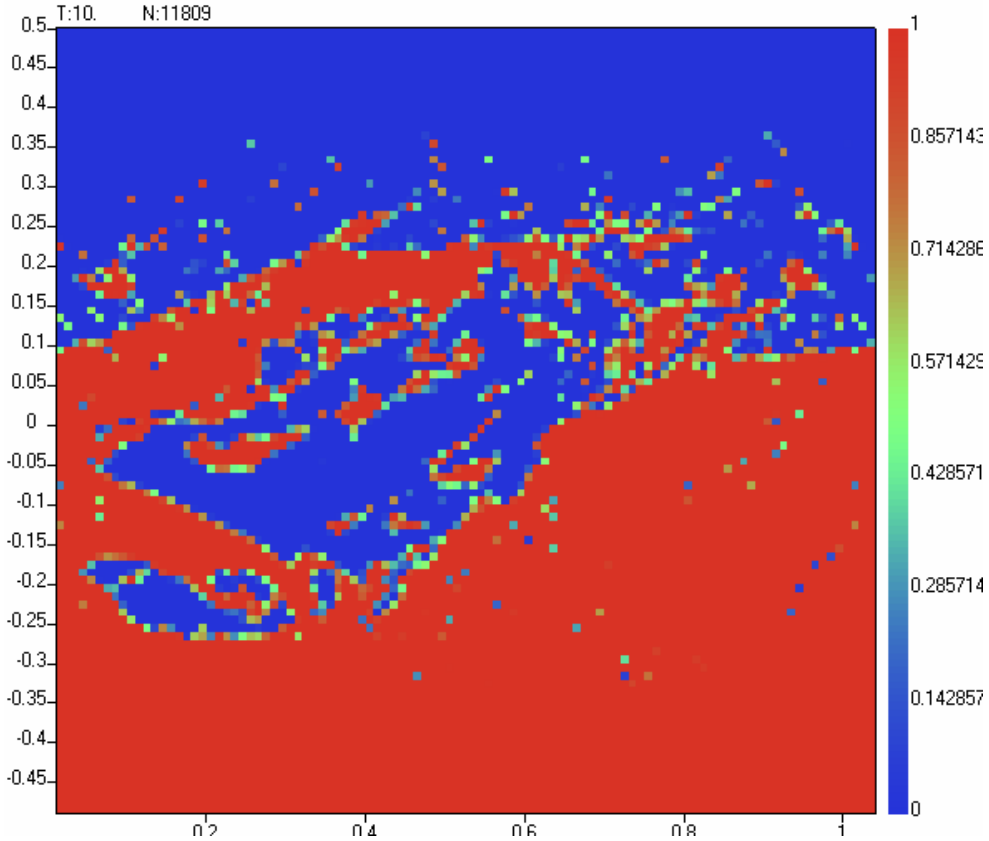

τ=2

Fig. 2. Raster patterns of the heavy material concentration in the 3D computation on grid N_x=100

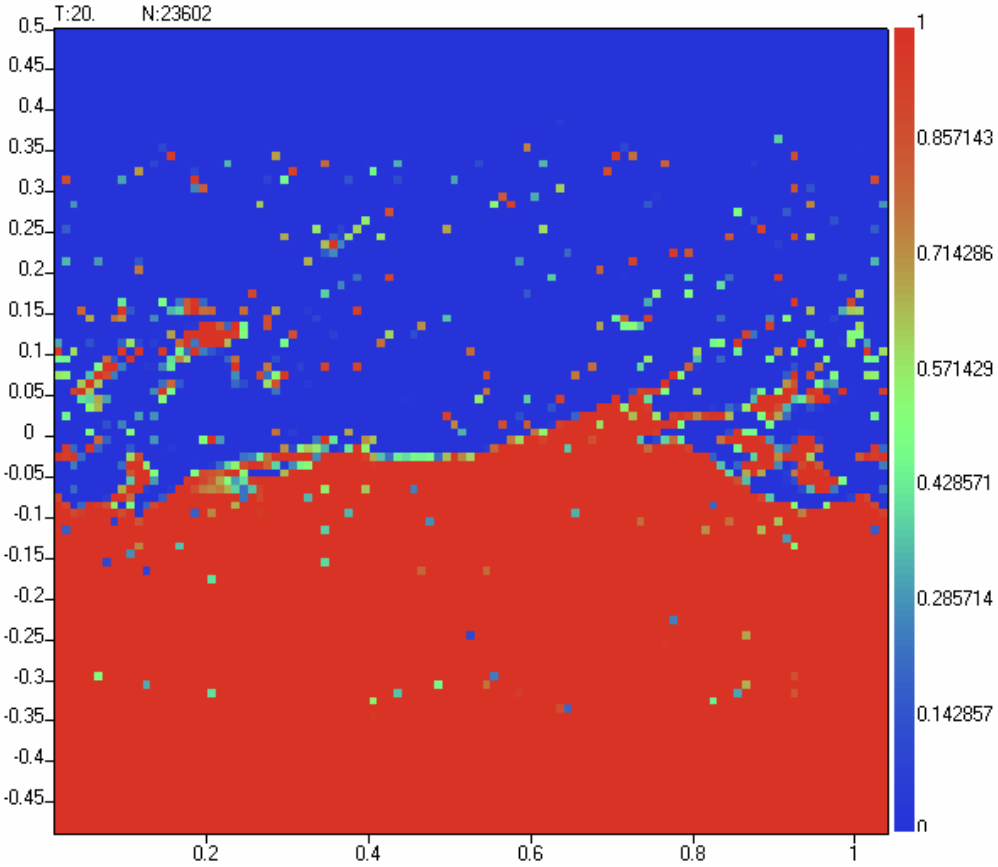

Fig. 3. Raster patterns of the heavy material concentration in the 3D computation on grid N_x=100, τ=4

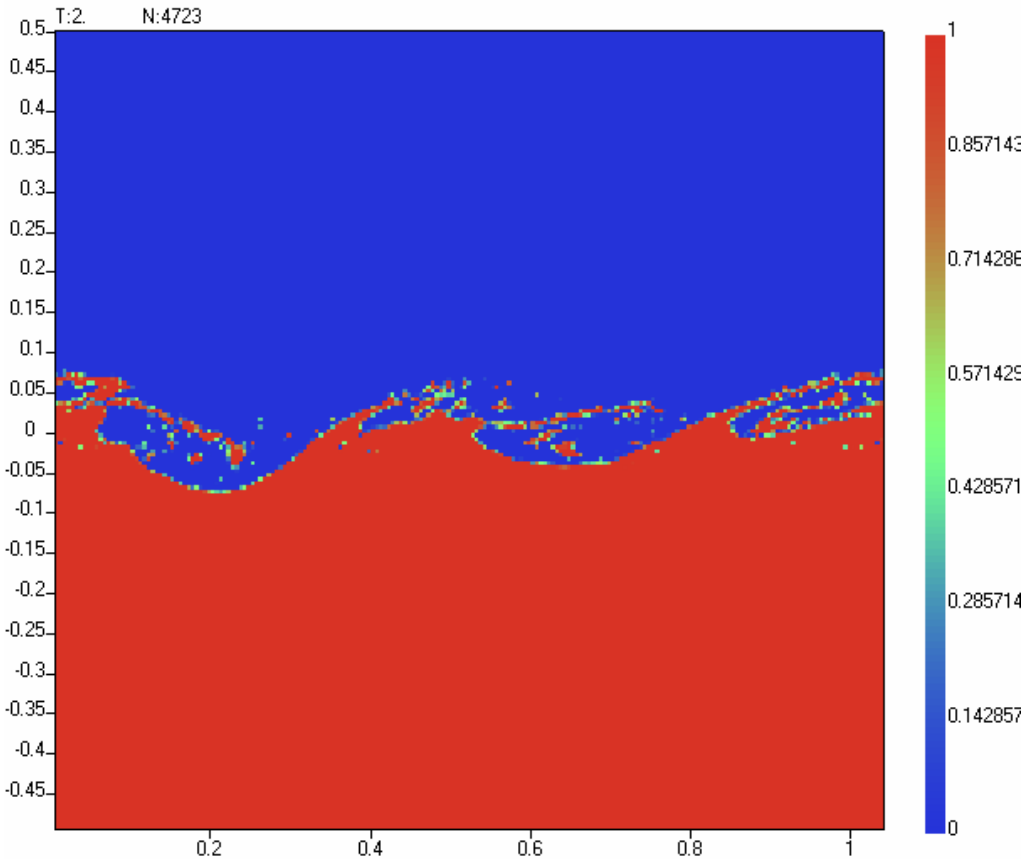

Fig. 4. Raster patterns of the heavy material concentration in the 3D computation on grid N_x=200, τ=0.4

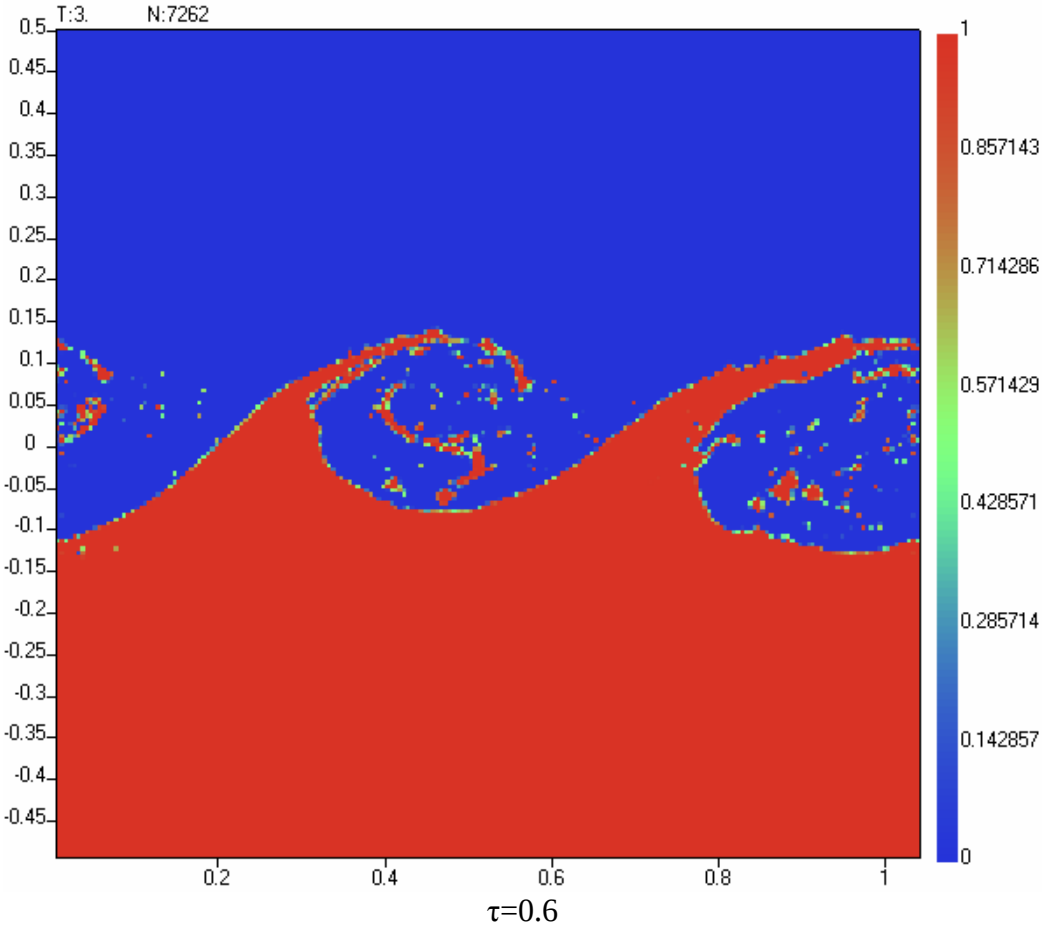

τ=0.6

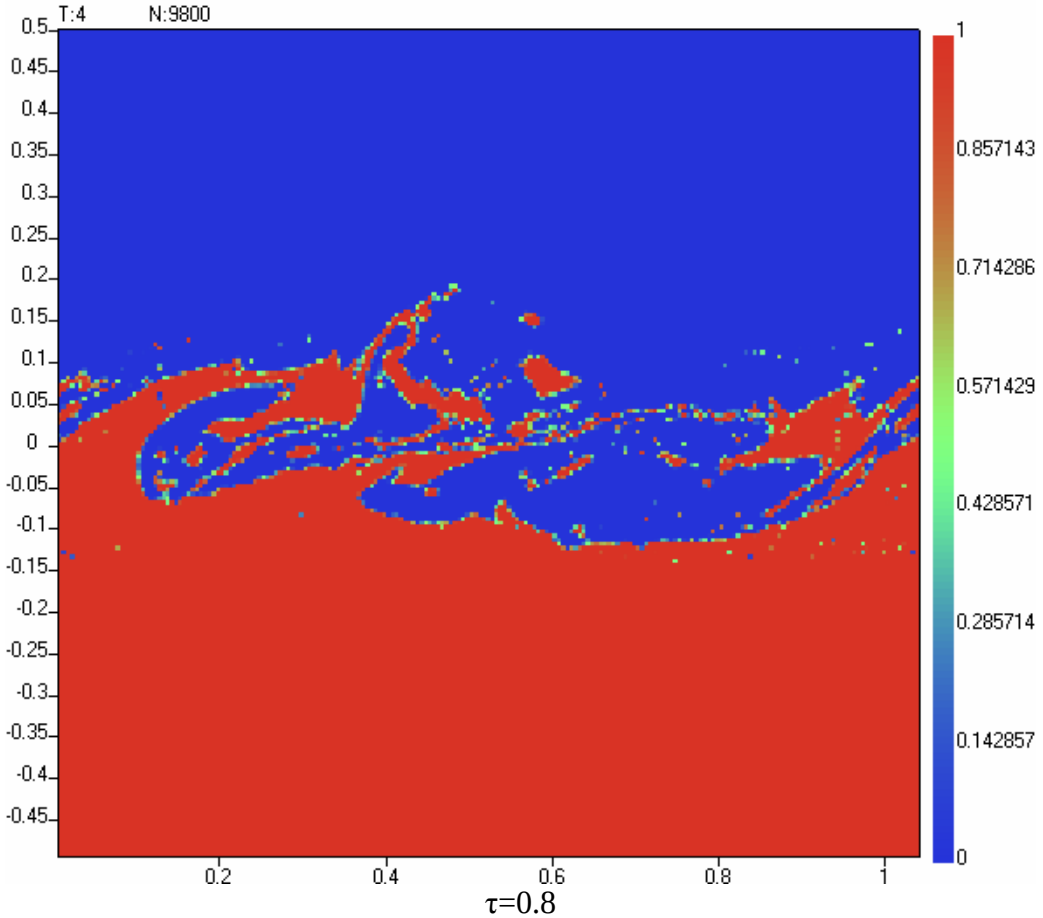

τ=0.8

Fig. 5. Raster patterns of the heavy material concentration in the computation on grid N_x=200

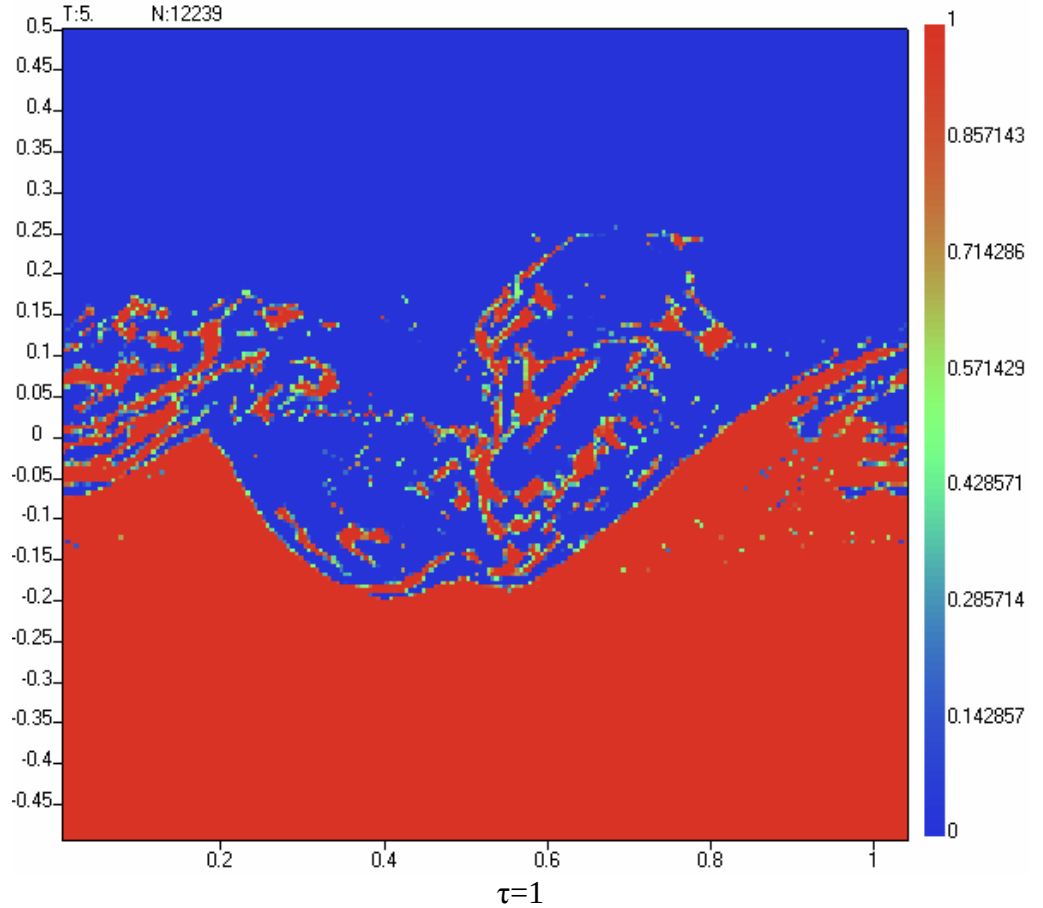

τ=1

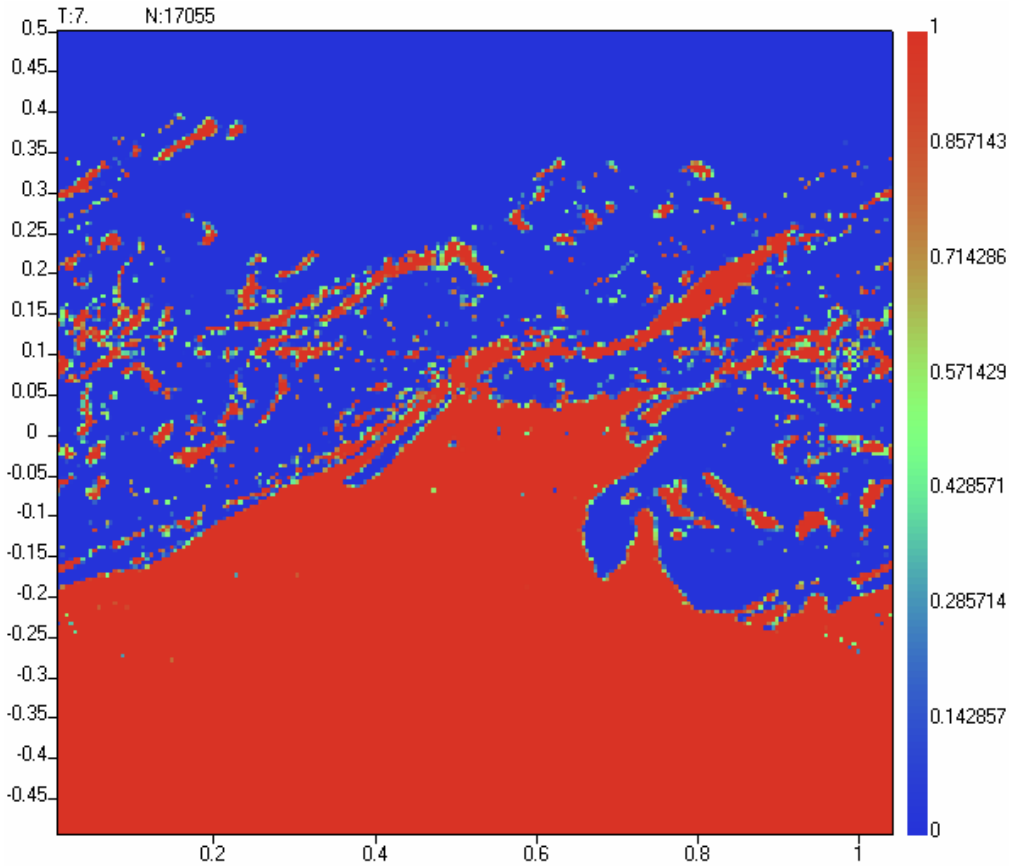

τ=1.4

Fig. 6. Raster patterns of the heavy material concentration in the 3D computation on grid N_x=200

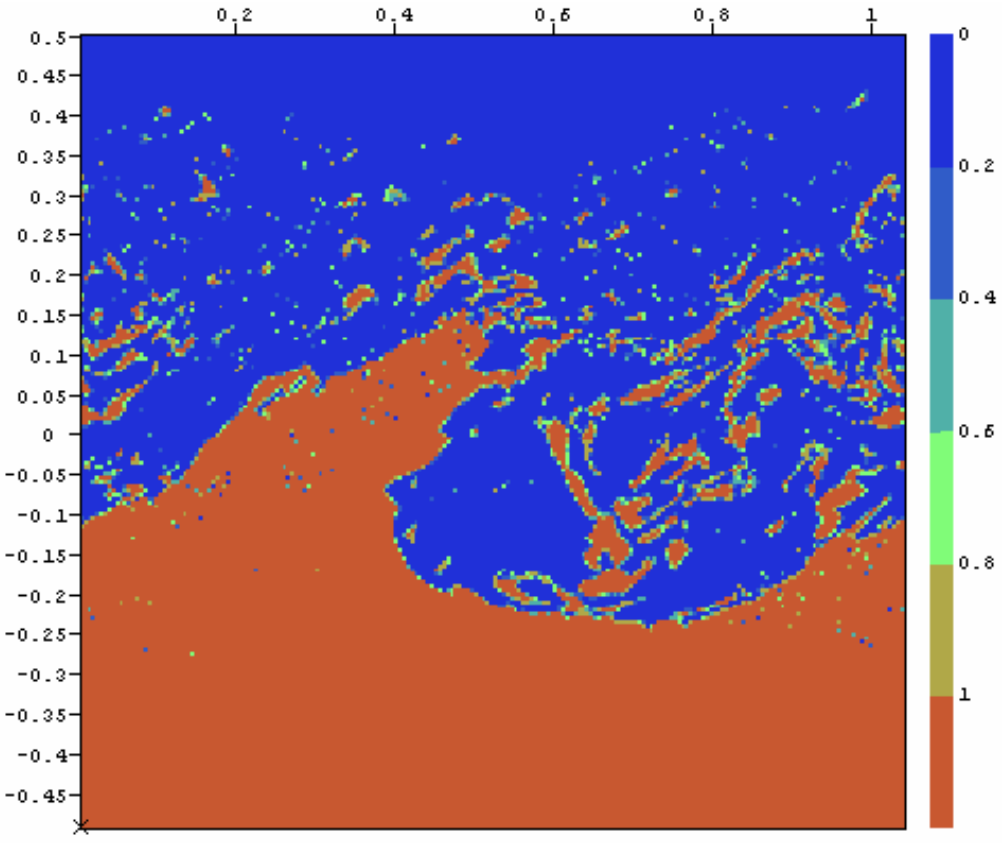

τ=1.6

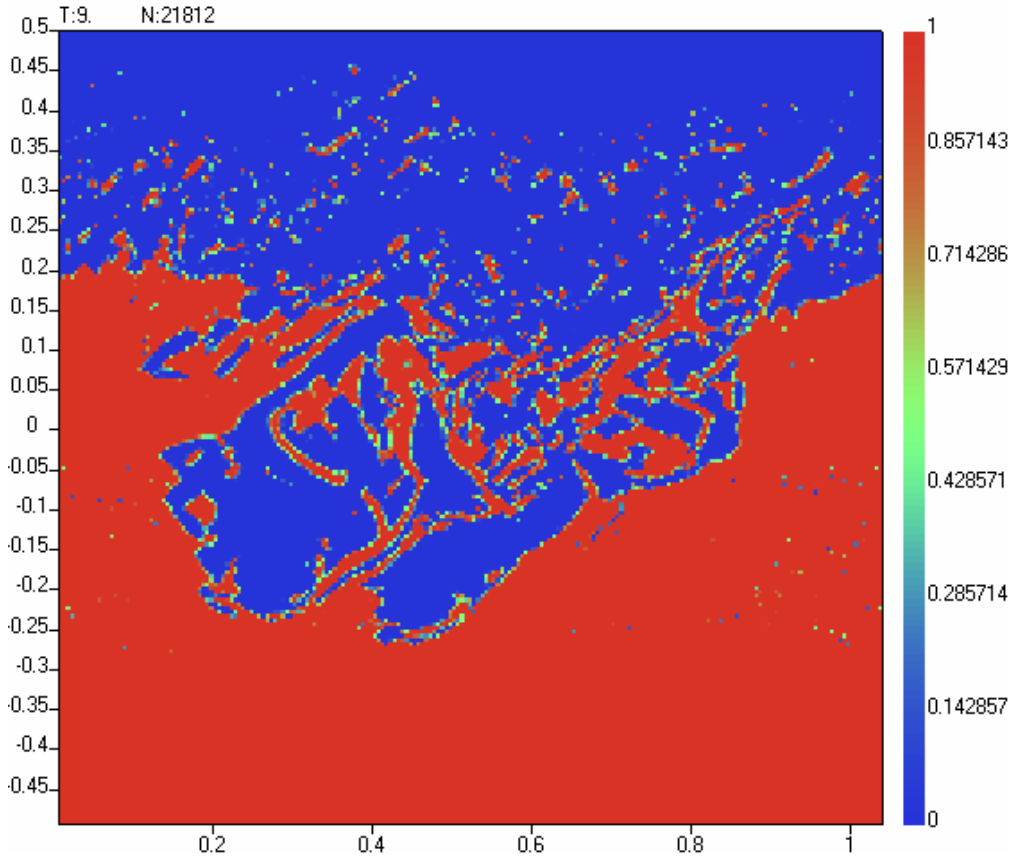

τ=1.8

Fig. 7. Raster patterns of the heavy material concentration in the 3D computation on grid N_x=200

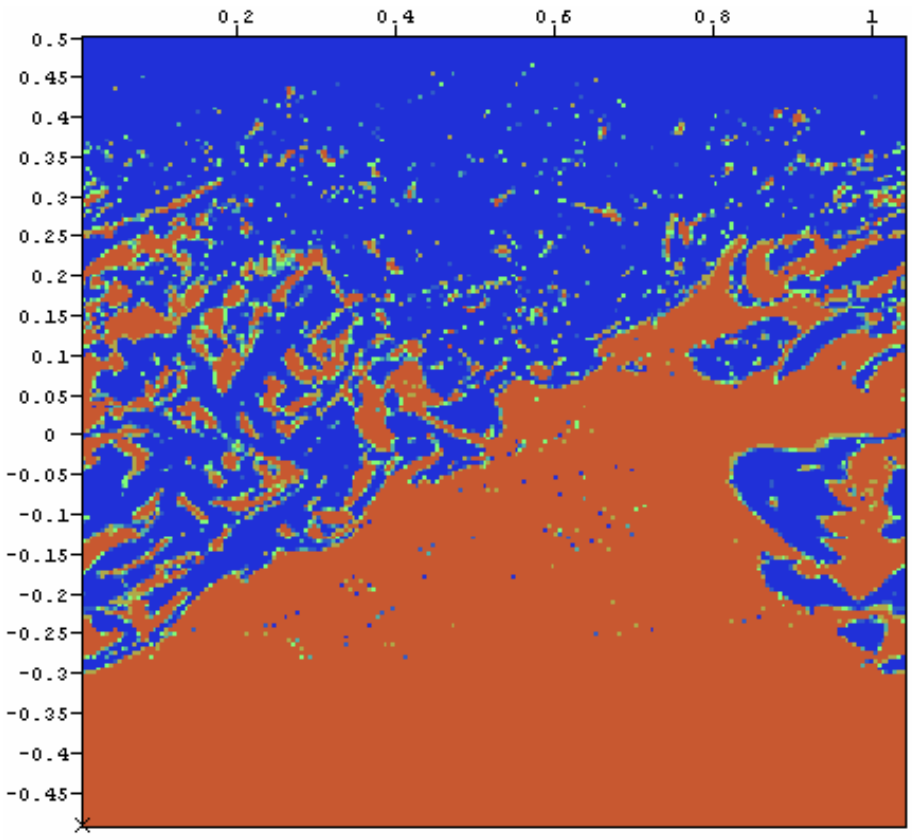

τ=2

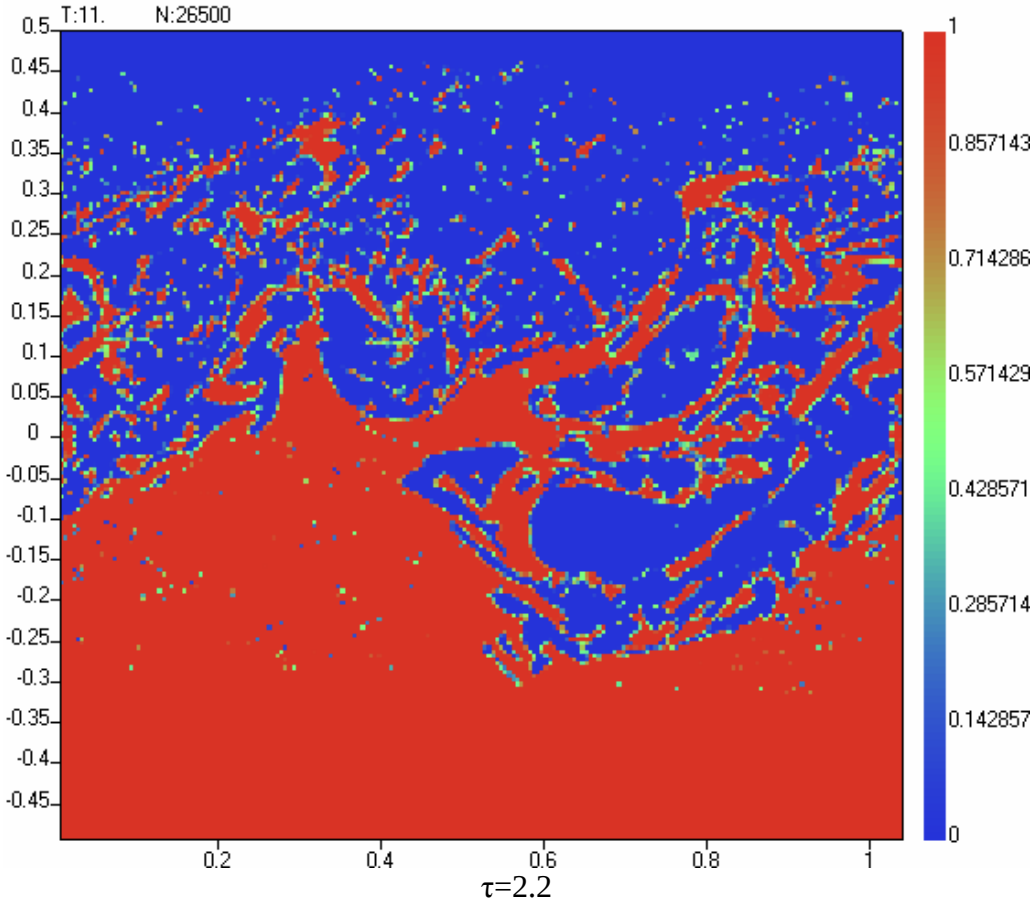

τ=2.2

Fig. 8. Raster patterns of the heavy material concentration in the 3D computation on grid N_x=200

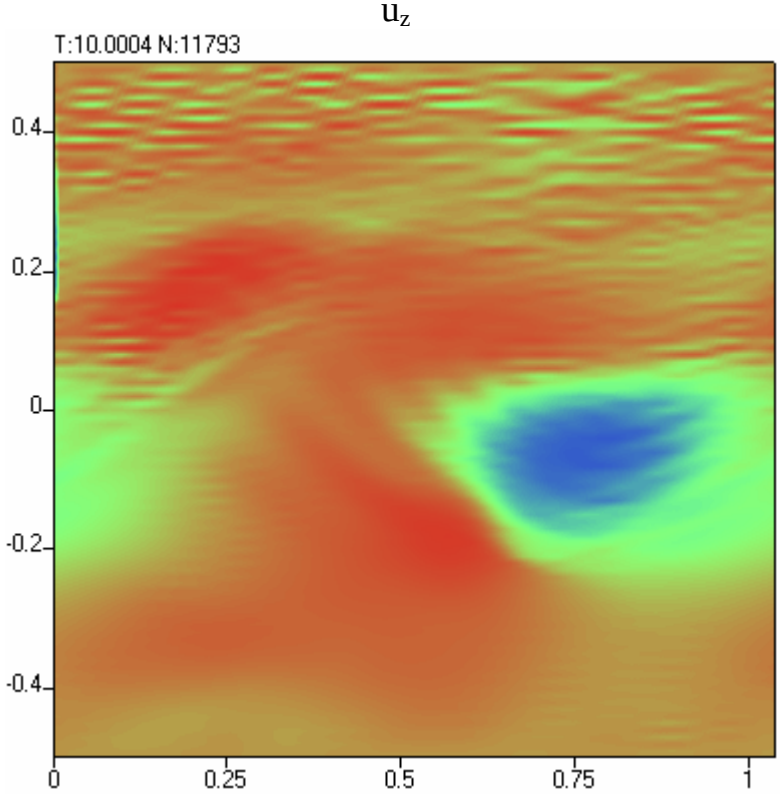

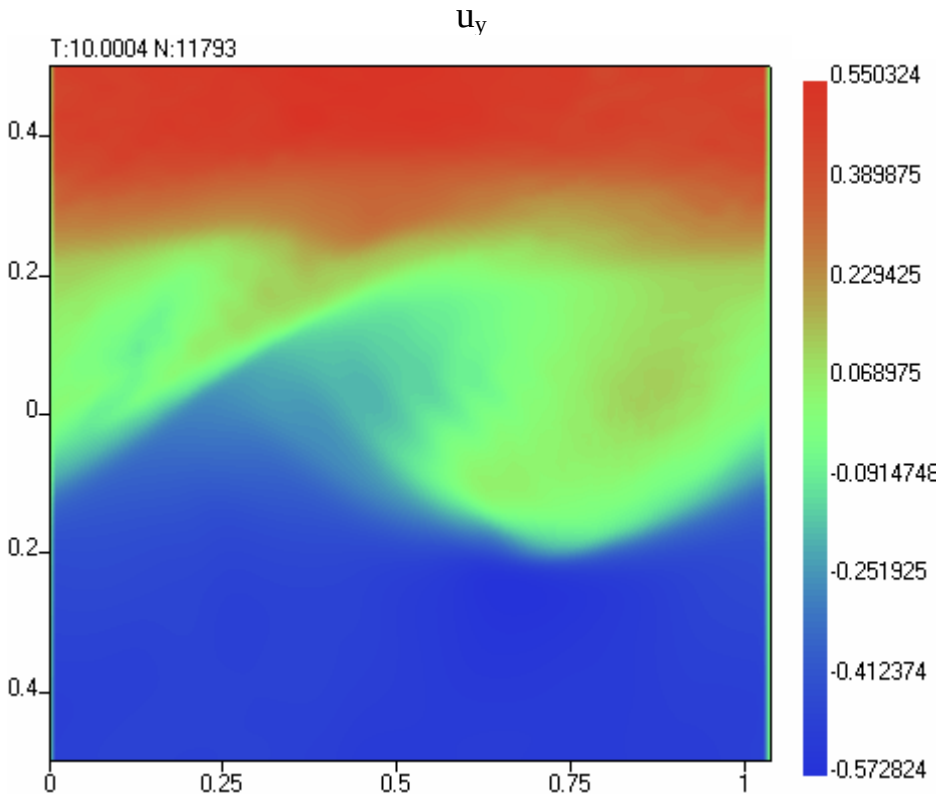

Fig. 9. Raster patterns of the velocity components in the 3D computation on grid N_x=100 (single material), τ=2

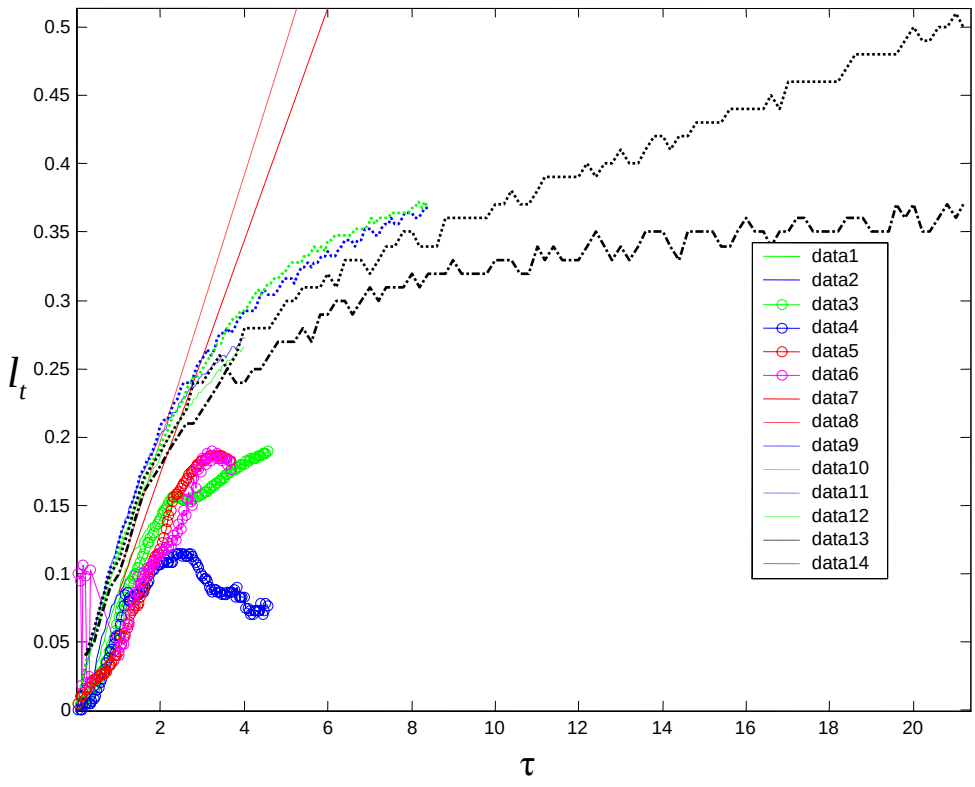

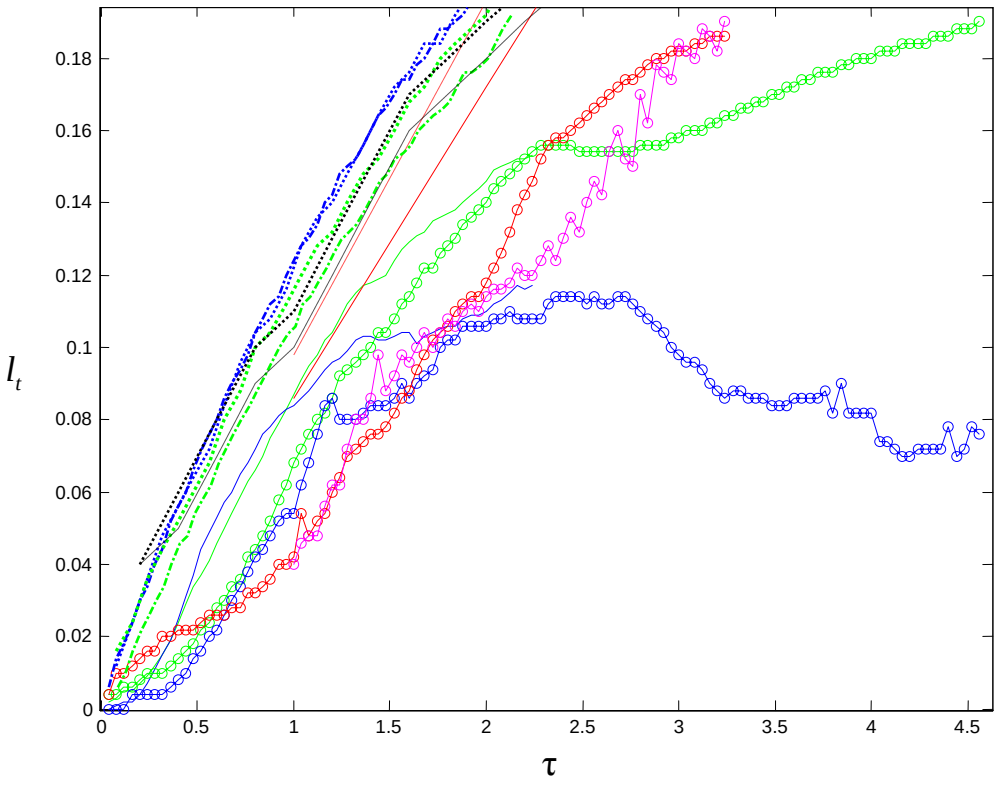

Fig. 10. TMZ width versus time. $l_t^{(u)}$: 1 – 3D computation with N_x=200, 3 - 3D computation with N_x=100, 5 - 3D computation with N_x=100, one material, 10 - 1D computation with g=0.2, 12 - 1D computation with g=0.4, 14 - 1D computation with g=1. $l_t^{(c)}$: 2, 4, 6, 9, 11, 13 – in the relevant variants. 7,8 – approximation to experimental data [7-9].

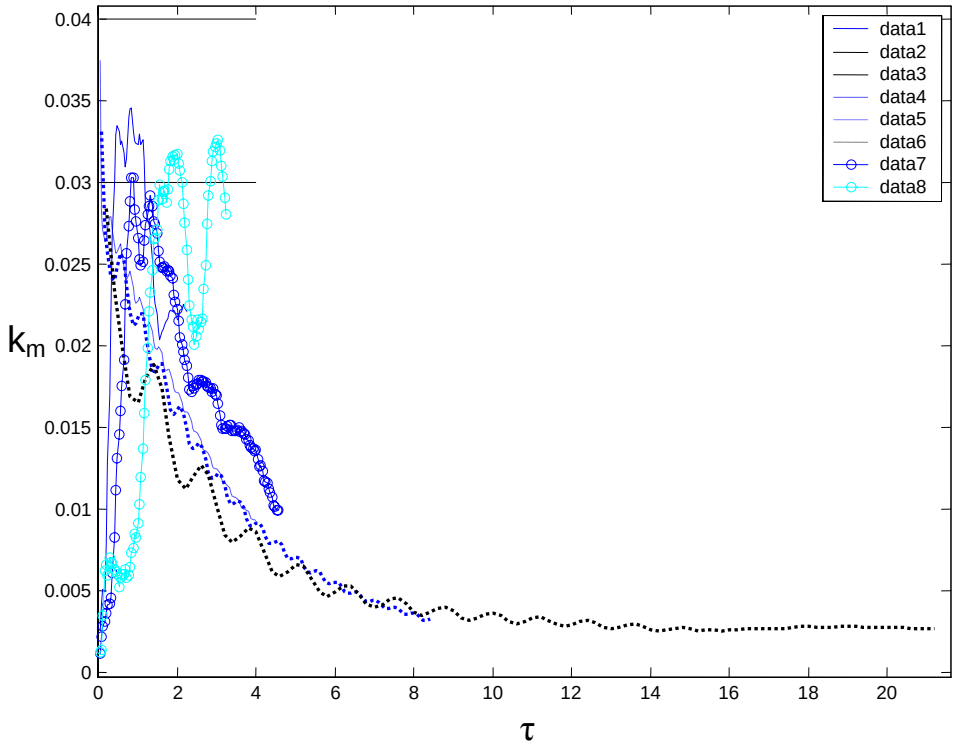

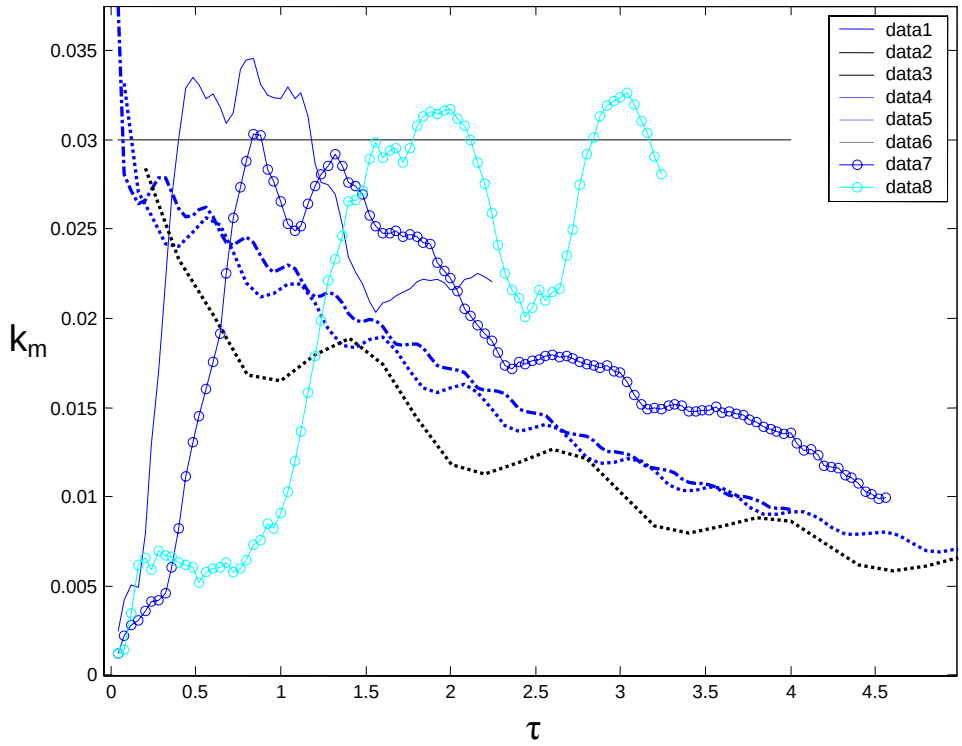

Fig. 11. TMZ-maximum turbulent energy versus time. 1 – 3D computation with N_x=200, 7 - 3D computation with N_x=100, 8 - 3D computation with N_x=100, one material, 4 - 1D computation with g=0.2, 5 - 1D computation with g=0.4, 6 - 1D computation with g=1. 2,3 – approximation to experimental data [7,8]

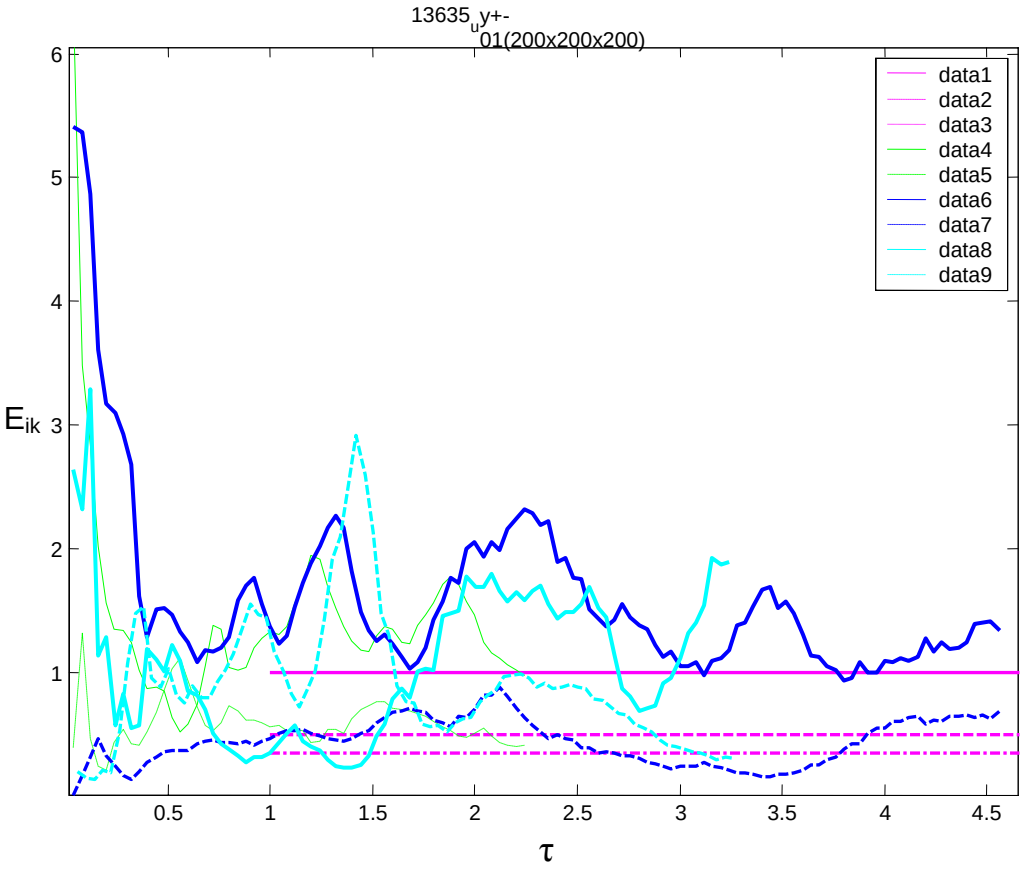

Fig. 12. Velocity fluctuation anisotropy versus time. The analytical solution for the initial stage: 1 - E_{xz}, 2 - E_{zy}, b=0.085; 3 - E_{zy}, b=0.13; 3D computations: 4,6,8 - E_{xz}, 5,7,9 E_{zy}; 4,5 – 3D computation with N_x=200, 6,7 - 3D computation with N_x=100, 8,9 - 3D computation with N_x=100, one material

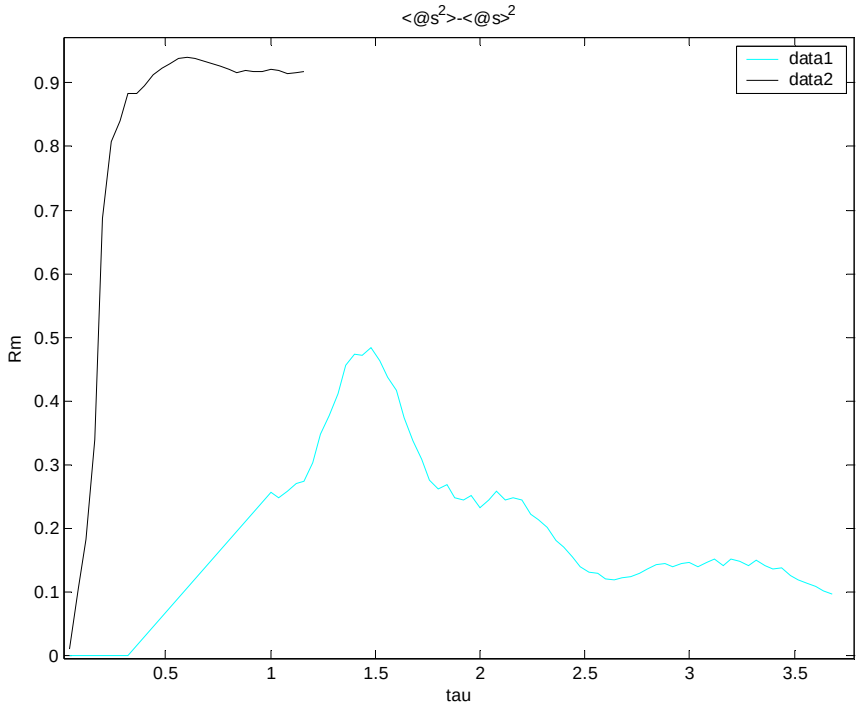

Fig. 13. TMZ-maximum squared density fluctuation versus time

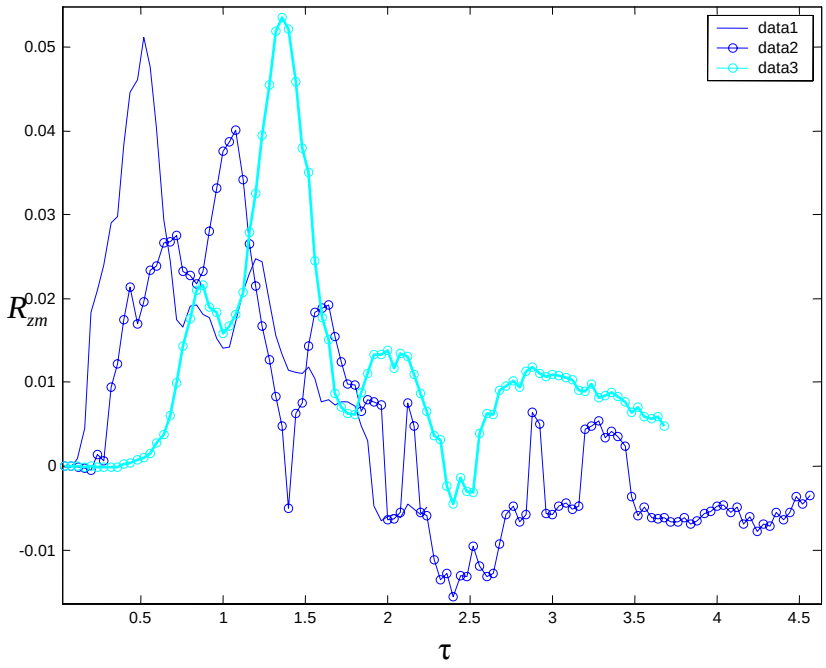

Fig. 14. TMZ-maximum (modulo) turbulent mass flow versus time in the computations: 1 – N_x =200, 2 - N_x =100, 3 - N_x =100, one material

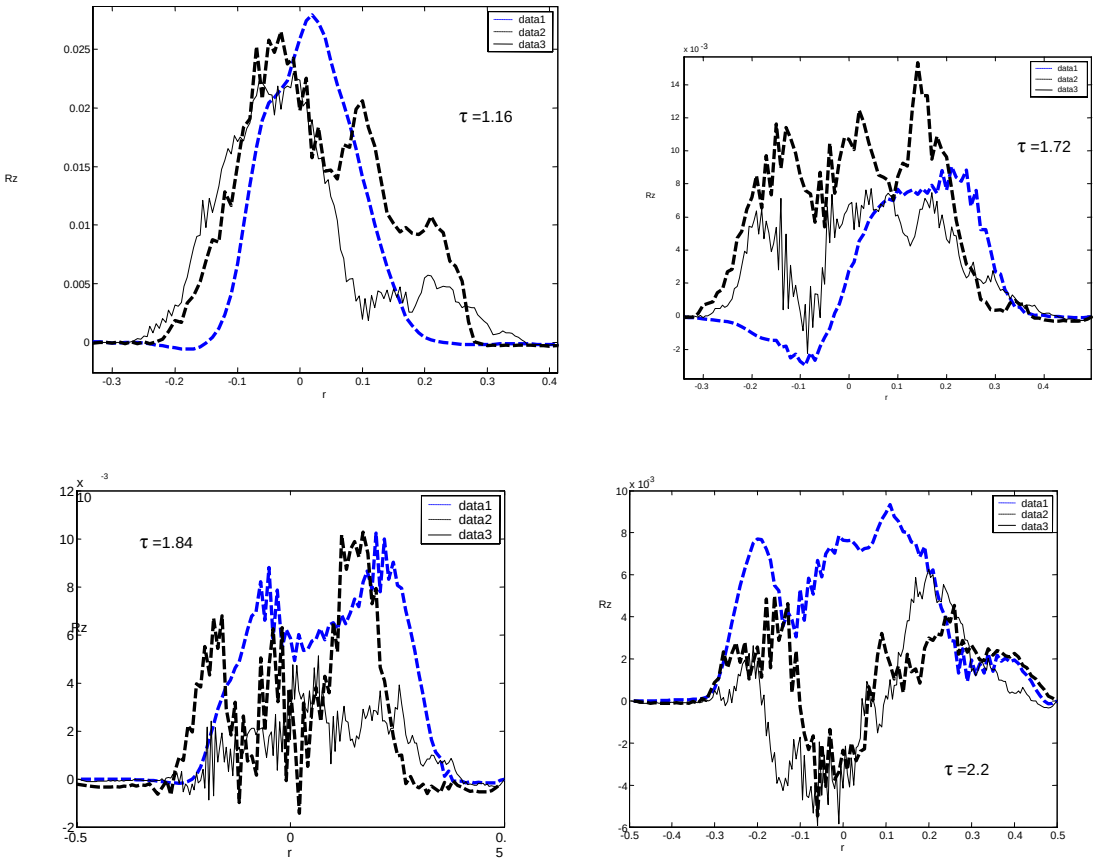

Fig. 15. Turbulent mass flow profiles in the 3D computations: 1- N_x =100, one material, 2 - N_x =100, two materials, 3 - N_x =200, two materials

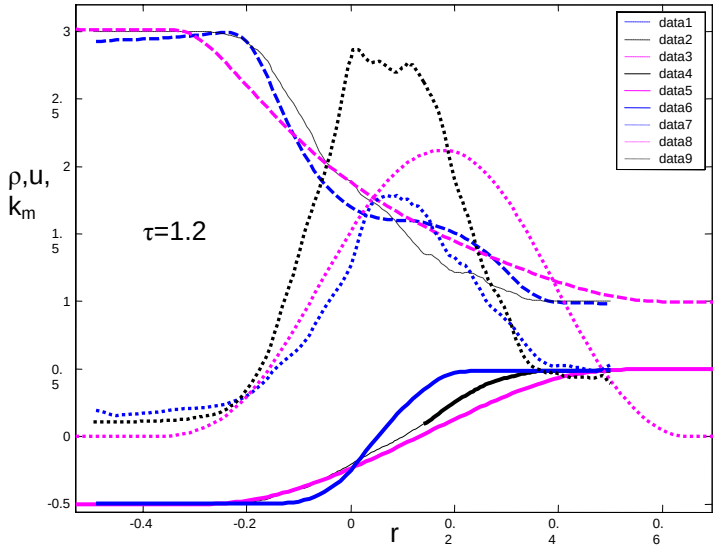

(a)

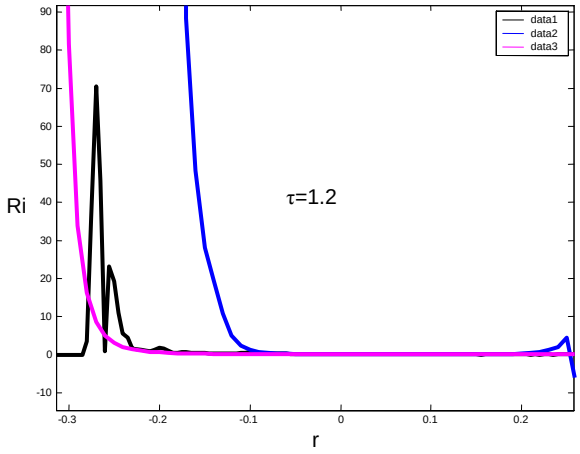

(b)

Fig. 16. τ=1.2. a) rofiles of velocity (1-3), density (4-6), turbulent energy (7-9); 1,6,7 - N_x=100, one material, 2,4,8 - N_x=200, two materials, 3,5,9 - $k-\varepsilon$ model. b) Ri number profiles; 1 - N_x=200, two materials, 2 - N_x=100, one material, 3 - $k-\varepsilon$ model

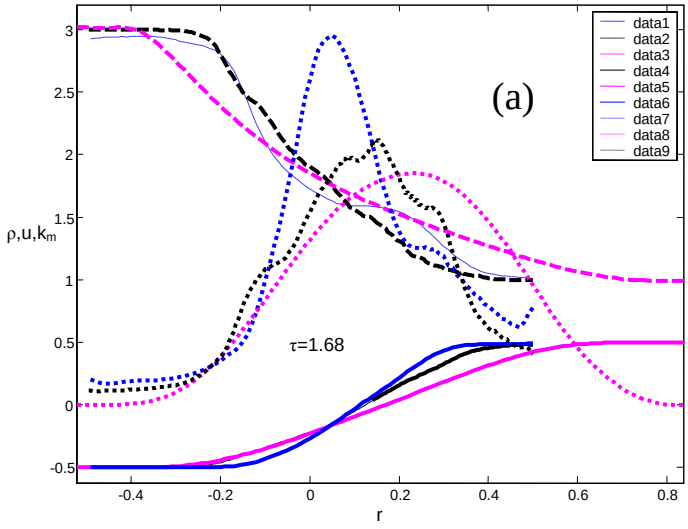

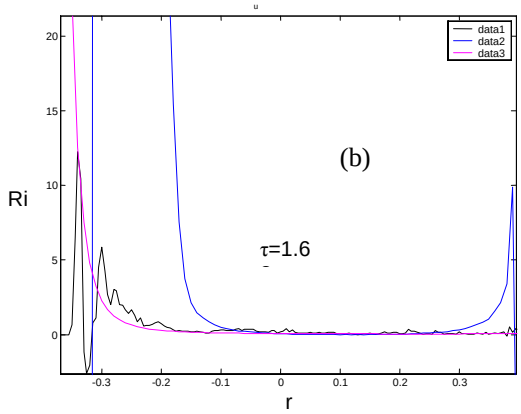

Fig. 17. τ=1.68. a) Profiles of velocity (1-3), density (4-6), turbulent energy (7-9); 1,6,7 - N_x=100, one material, 2,4,8 - N_x=200, two materials, 3,5,9 - $k-\varepsilon$ model. b) Richardson number profiles; 1 - N_x=200, two materials, 2 - N_x=100, one material, 3 - $k-\varepsilon$ model

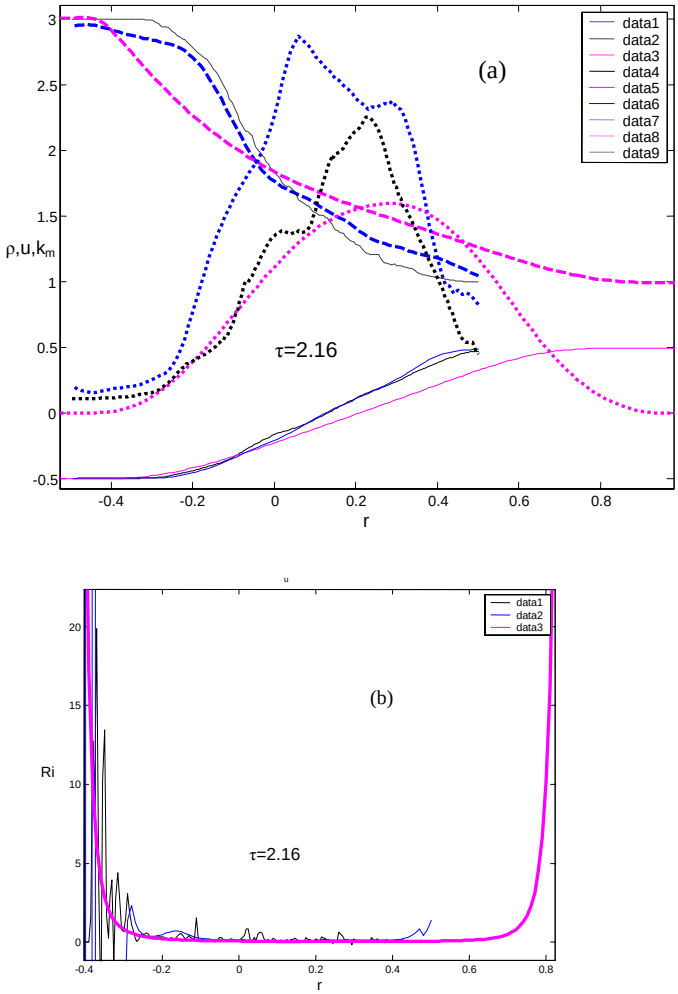

Fig. 18. τ=2.16. a) Profiles of velocity (1-3), density (4-6), turbulent energy(7-9); 1,6,7 - N_x=100, one material, 2,4,8 - N_x=200, two materials, 3,5,9 - $k-\varepsilon$ model. b) Richardson number profiles; 1 - N_x=200, two materials, 2 - N_x=100, one material, 3 - $k-\varepsilon$ model

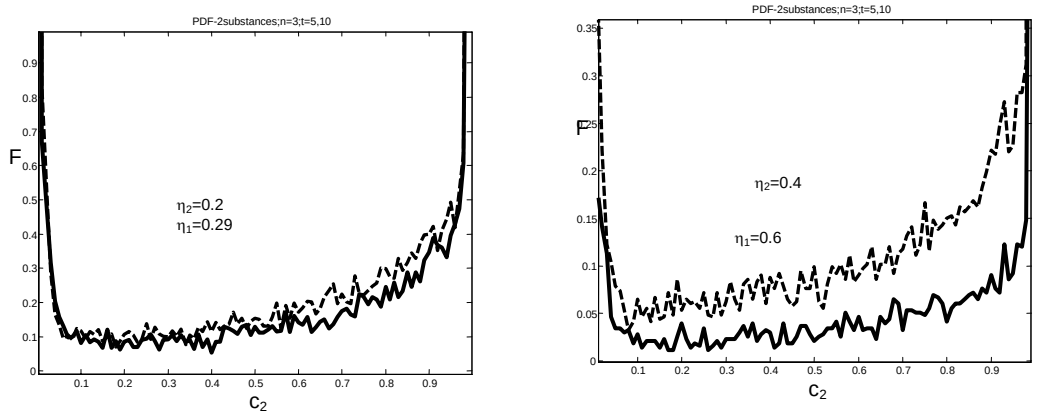

Fig. 19. Heavy material mass concentration probability distribution density function in the 3D computation (without initial concentration array averaging) on grid N_x=200, two materials. 1- τ=1, 2 - τ=2

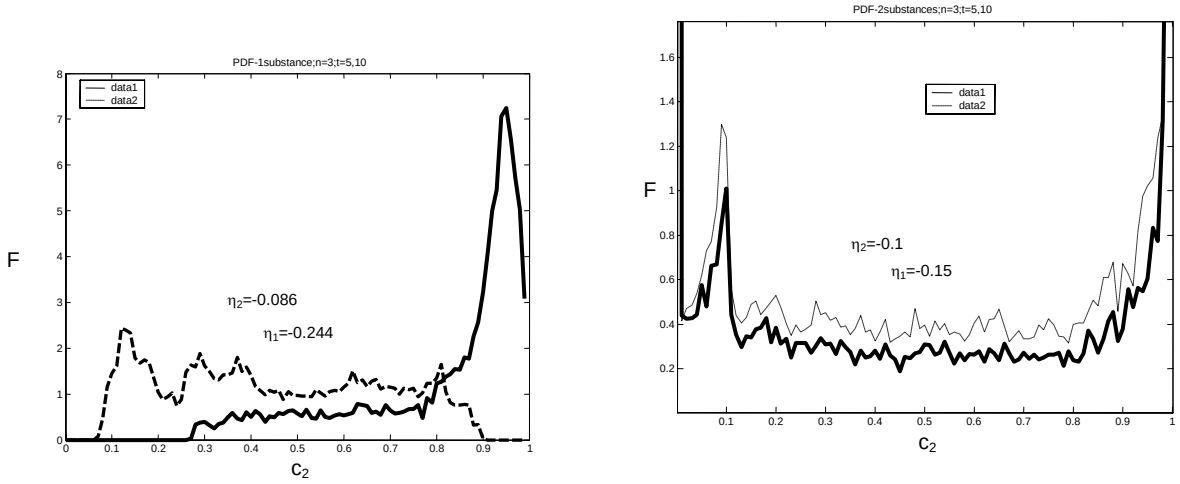

a) b)

Fig. 20. Heavy material mass concentration probability distribution density function in the 3D computations (with initial concentration array averaging, r=2): a) – grid N_x=100, one material, b) - grid N_x=200, two materials. 1- τ=1, 2 - τ=2

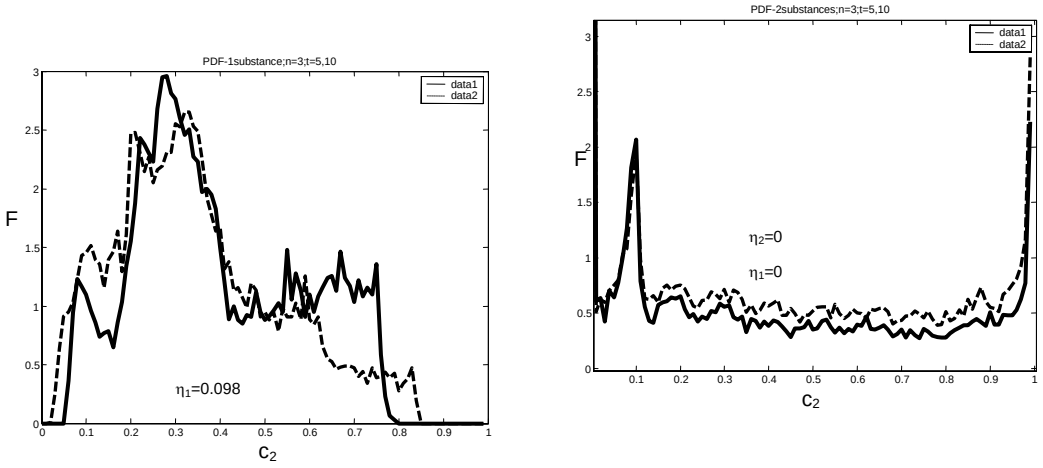

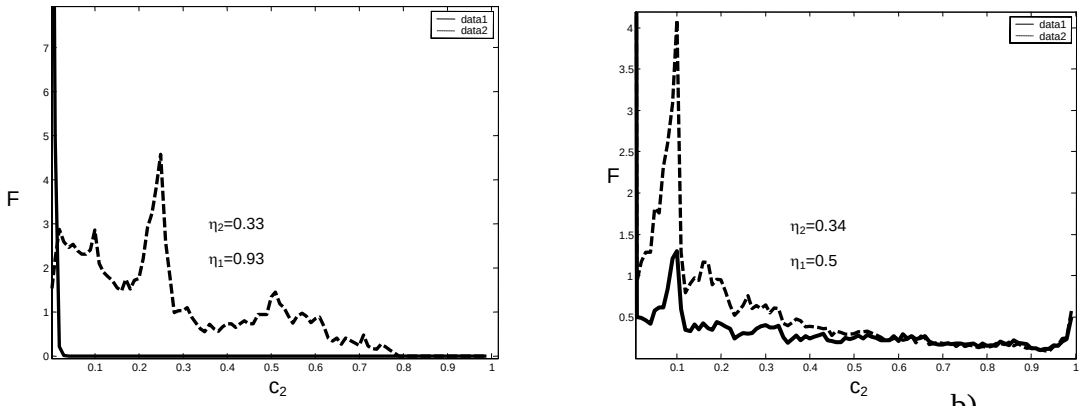

Fig. 21. Heavy material mass concentration probability distribution density function in the 3D computations (with initial concentration array averaging, r=2): a) – grid N_x=100, one material, b) - N_x=200, two materials. 1- τ=1, 2 - τ=2

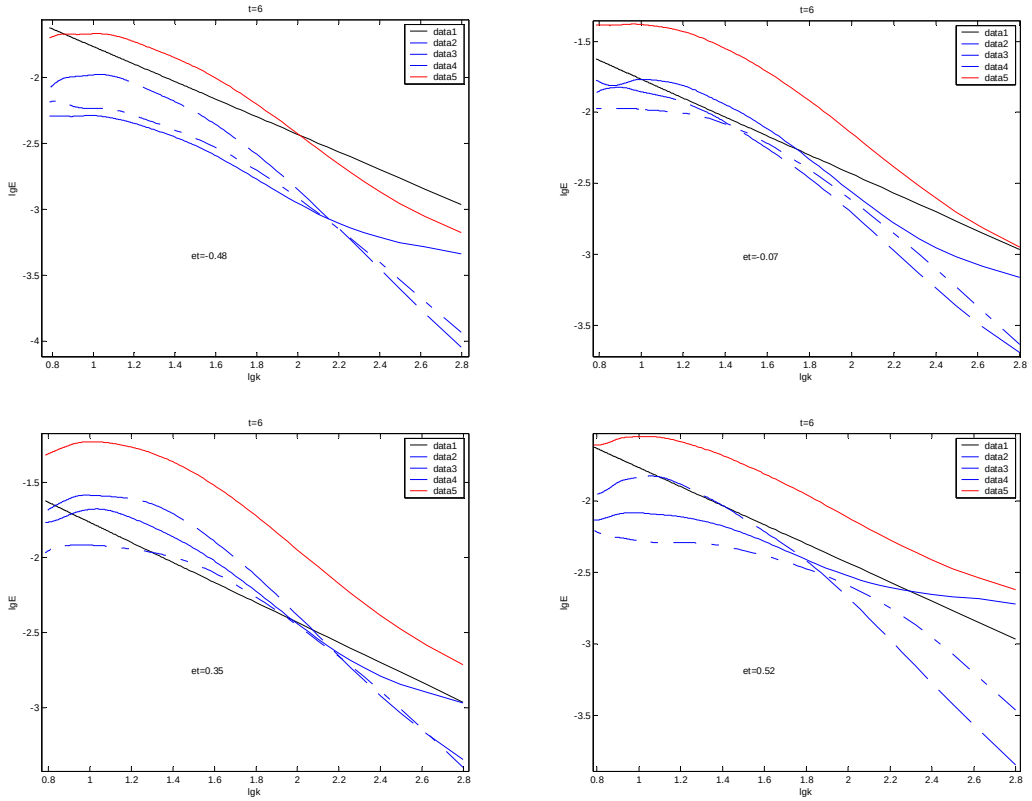

Fig. 22. Spectrum of the turbulent energy and its components in the computation on grid N_x=200, τ=1.2; 2 - E_x, 3 - E_y, 4 - E_z, 5 – E; 1 - Kolmogorov spectrum

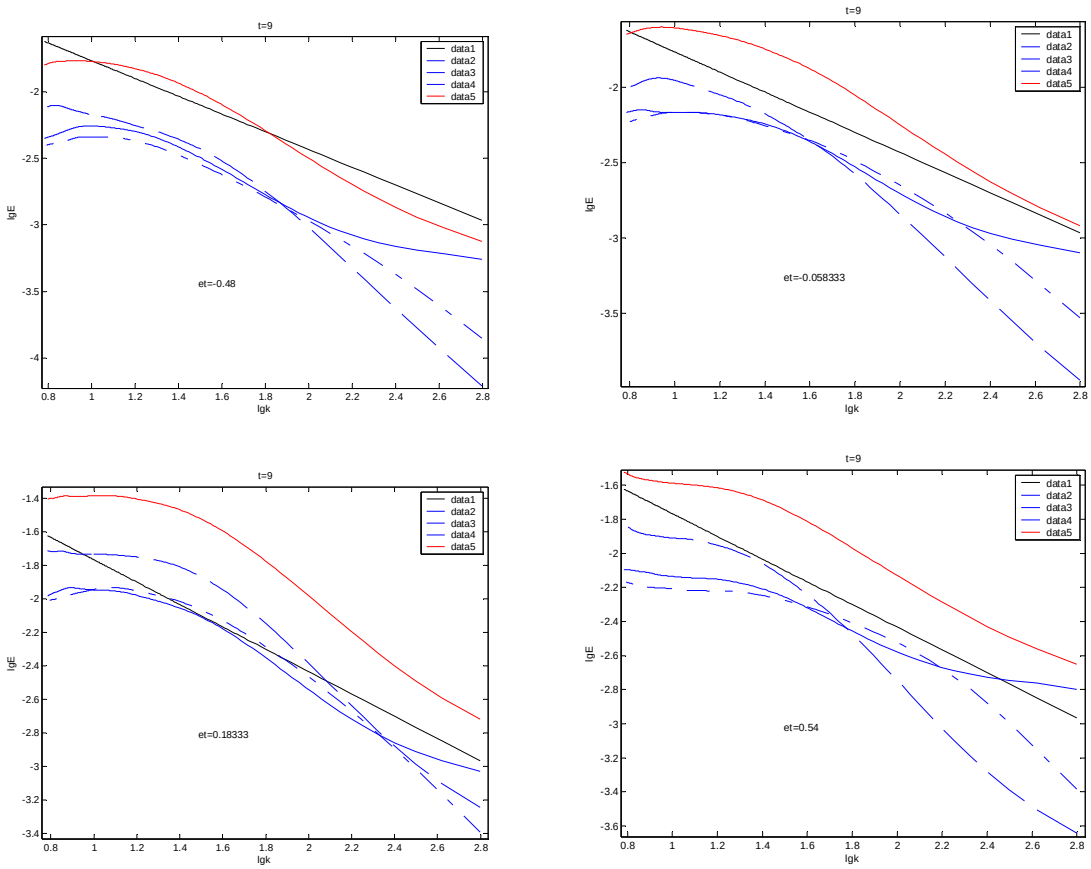

Fig. 23. Spectrum of the turbulent energy $E(k)$ and its components $E_i(k)$ in the computation on grid N_x=200, τ=1.8; 2 - E_x, 3 - E_y, 4 - E_z, 5 – E; 1 - Kolmogorov spectrum

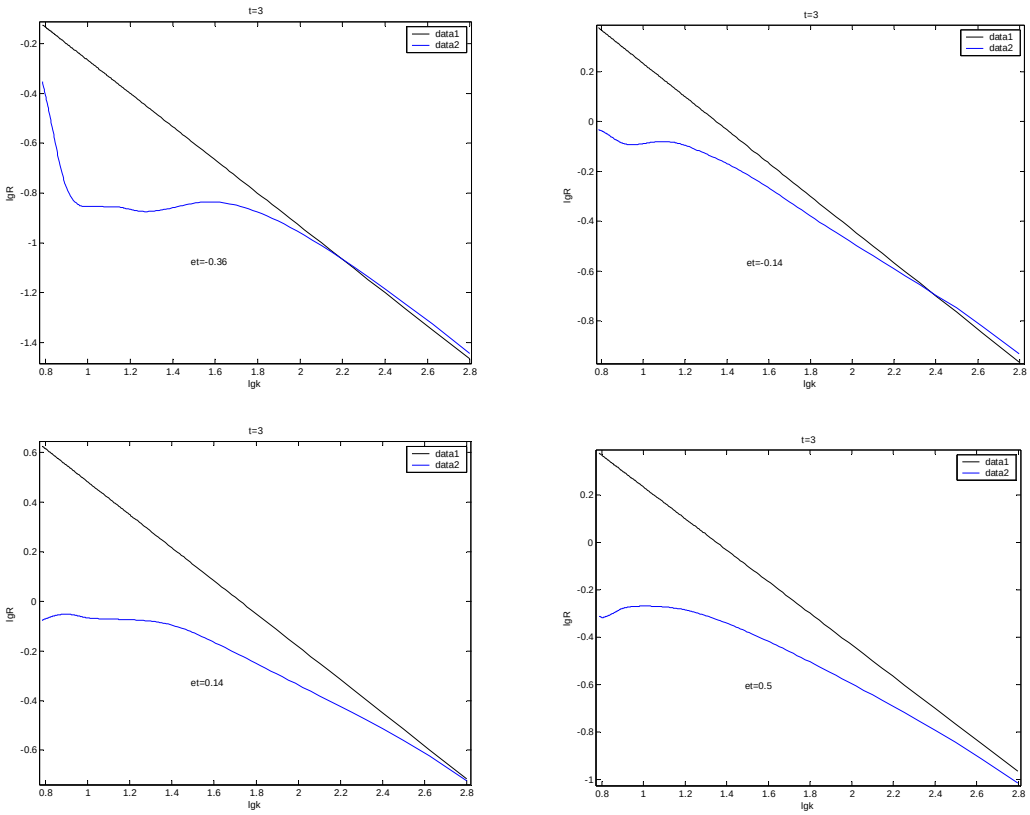

Fig. 24 Spectrum of the density fluctuations R_l in the 3D computation on grid N_x=200, τ=0.6; 1 - Kolmogorov spectrum, 2 –computation

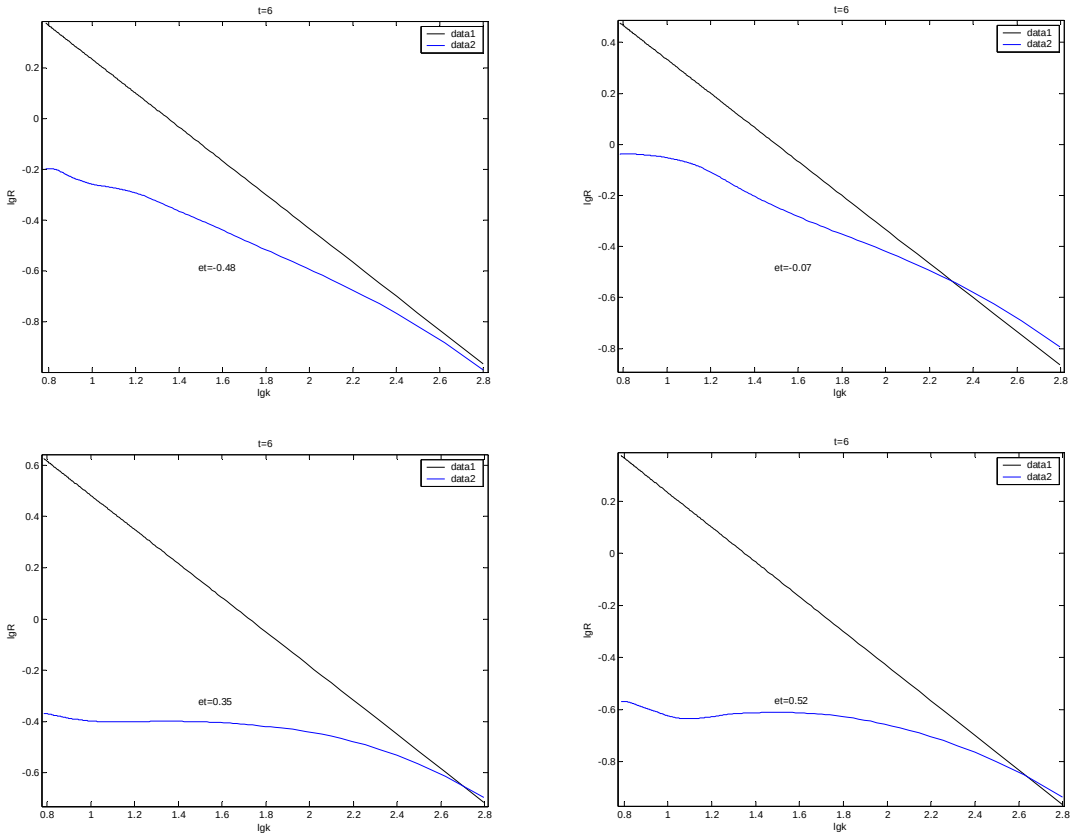

Fig. 25. Spectrum of the density fluctuations R_l in the 3D computation on grid N_x=200, τ=1.2; 1 - Kolmogorov spectrum, 2 –computation

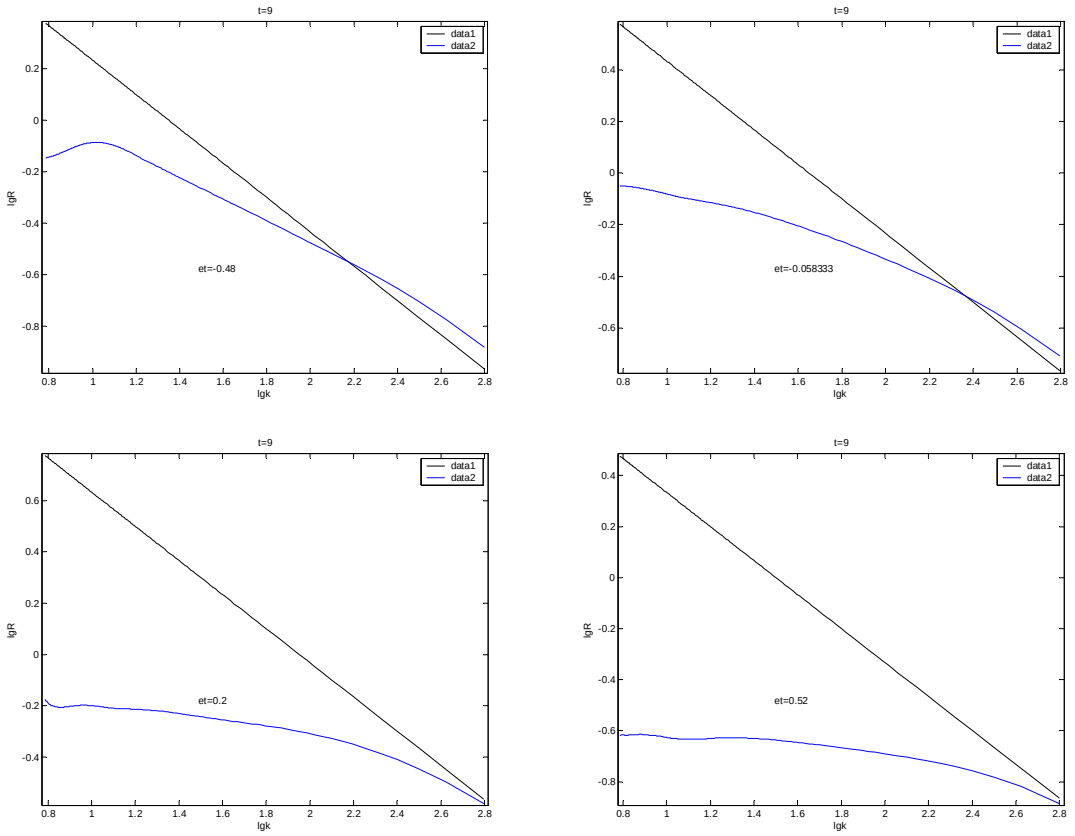

Fig. 26.Spectrum of the density fluctuations R_l in the 3D computation on grid N_x=200, τ=1.8; 1 - Kolmogorov spectrum, 2 –computation